Since January 2020 Elsevier has created a COVID-19 resource centre with free information in English and Mandarin on the novel coronavirus COVID-19. The COVID-19 resource centre is hosted on Elsevier Connect, the company's public news and information website.

BBA - Biomembranes 1864 (2022) 183945

Contents lists available at ScienceDirect

BBA - Biomembranes

journal homepage: www.elsevier.com/locate/bbamem

Amphiphilic anti-SARS-CoV-2 drug remdesivir incorporates into the lipid bilayer and nerve terminal membranes influencing excitatory and inhibitory neurotransmission

Natalia Krisanova [a], Natalia Pozdnyakova [a], Artem Pastukhov [a], Marina Dudarenko [a], Oleg Shatursky [a], Olena Gnatyuk [b], Uliana Afonina [b], Kyrylo Pyrshev [a], Galina Dovbeshko [b], Semen Yesylevskyy [b,c], Tatiana Borisova [a,*]

[a] The Department of Neurochemistry, Palladin Institute of Biochemistry, NAS of Ukraine, 9 Leontovicha Str., Kyiv 01054, Ukraine
[b] The Department of Physics of biological systems, Institute of Physics, NAS of Ukraine, 46 Nauky Ave., Kyiv 03680, Ukraine
[c] Laboratoire Chrono Environnement UMR CNRS 6249, Université de Bourgogne Franche-Comté, 16 route de Gray, 25030 Besançon Cedex, France

ARTICLE INFO

Keywords:
COVID-19
Anti-SARS-COV-2 drug
Antiviral drug
Amphiphilicity
Synaptic neurotransmission
Excitation
Inhibition
Exocytosis
Synaptic vesicle acidification
Brain nerve terminals
Molecular dynamics simulations
FTIR spectroscopy
Planar phospholipid bilayer membranes

ABSTRACT

Remdesivir is a novel antiviral drug, which is active against the SARS-CoV-2 virus. Remdesivir is known to accumulate in the brain but it is not clear whether it influences the neurotransmission. Here we report diverse and pronounced effects of remdesivir on transportation and release of excitatory and inhibitory neurotransmitters in rat cortex nerve terminals (synaptosomes) in vitro. Direct incorporation of remdesivir molecules into the cellular membranes was shown by FTIR spectroscopy, planar phospholipid bilayer membranes and computational techniques. Remdesivir decreases depolarization-induced exocytotic release of L-[^{14}C] glutamate and [^{3}H] GABA, and also [^{3}H] GABA uptake and extracellular level in synaptosomes in a dose-dependent manner. Fluorimetric studies confirmed remdesivir-induced impairment of exocytosis in nerve terminals and revealed a decrease in synaptic vesicle acidification. Our data suggest that remdesivir dosing during antiviral therapy should be precisely controlled to prevent possible neuromodulatory action at the presynaptic level. Further studies of neurotropic and membranotropic effects of remdesivir are necessary.

1. Introduction

Various viruses may cross the blood brain barrier and enter the central nervous system, causing, triggering or worsening neuronal impairment, psychiatric disorders and neurodegenerative diseases [1]. Neurotropism is a common feature of large enveloped RNA viruses, such as coronaviruses. Particularly, SARS-CoV-2 infection is often accompanied with neurological symptoms, such as dizziness (7.6–46.1%), impaired consciousness (9.5–64.1%), and seizures (1.2–26%) [2]. The coronaviruses were reveled in different brain regions in patients and experimental animals [3–5]. The brain was a main target organ for infection in mice transgenic for ACE2 [3], and MERS virus particles were identified only in the brain in the mice infected by low inoculum doses [4,5]. HEV 67N virus is transferred between neurons using the clathrin-dependent endocytotic/exocytotic pathway and the trans-synaptic transfer has been established for various CoVs [5,6], which may first attack the peripheral nerve terminals, and then the central nervous system via synapses [3,5]. SARS-CoV-2 was found in the intracellular organelles, e.g. vesicles, of virus-infected Vero cells [7]. Animal death in SARS-CoV infection may result from dysfunction and death of infected neurons [3]. While neurological symptoms were widely reported for SARS-CoV-2 infection in human, its neuronal acute and long-term consequences are still unclear [1].

Due to the coronavirus pandemic and the absence of effective

Abbreviations: DMSO, Dimethyl sulfoxide; FCCP, carbonyl cyanide 4-(trifluoromethoxy)phenylhydrazone; GABA, γ-aminobutyric acid; HEPES, N-2-hydroxyethylpiperazine-n-2-ethane sulfonic acid; NO-711, 1,2,5,6-Tetrahydro-1-(2-(((diphenylmethylene)amino)oxy)ethyl)-3-pyridinecarboxylic acid hydrochloride; SEM, standard error of the mean; BLMs, planar phospholipid bilayer membranes.

* Corresponding author.
E-mail address: tborisov@biochem.kiev.ua (T. Borisova).

https://doi.org/10.1016/j.bbamem.2022.183945
Received 2 February 2022; Received in revised form 3 April 2022; Accepted 17 April 2022
Available online 22 April 2022

therapeutics for its treatment, a comprehensive study of potential anti-SARS-CoV-2 drugs is becoming especially important. Remdesivir (GS-5734) [8] is currently the only antiviral drug, which shows significant activity against SARS-CoV-2 and is FDA-authorised for emergency use for COVID-19 treatment [9]. Remdesivir was first developed as a novel monophosphoramidate prodrug of an adenosine analogue with antiviral activity against acute Ebola virus [10]. The pharmacologically active nucleoside triphosphate was efficiently formed in the cells incubated with remdesivir in vitro, and this nucleoside triphosphate acted as an alternative substrate and RNA-chain terminator for viral RNA polymerase [10]. Remdesivir is an amphiphilic molecule designed to easily cross the cellular plasma membrane in order to be rapidly metabolised intracellularly. In contrast, remdesivir active metabolite is not cell permeable [8]. Despite well-known propensity of remdesivir to incorporate and possible accumulate in the cell membranes there are no dedicated studies of its membranotropic action to date.

Pharmacokinetics, metabolism, and distribution of remdesivir were examined in nonhuman primates [10]. Intravenous administration of a 10 mg kg^{-1} dose of [^{14}C]GS-5734 in cynomolgus monkeys proved that the drug-derived material was distributed to eyes and brain within 4 h of administration. Levels of the drug and drug-derived material in the brain at 4 h after dose administration were approx. 7% relative to the plasma levels. 168 h after administration, the drug and drug-derived material in the brain remained detectable at the comparable levels [10]. Therefore, remdesivir distribution and pharmacokinetic studies revealed that it can be accumulated in the brain. Despite this finding, the capability of remdesivir to influence synaptic neurotransmission, which seems likely due to its membranotropism, was not studied yet.

In this study, we have assessed the effects of remdesivir on crucial characteristics of glutamate- and γ-aminobutyric acid (GABA)-ergic neurotransmission in isolated presynaptic rat cortex nerve terminals (synaptosomes), one of the best model systems to explore presynaptic processes [11].

Glutamate and GABA are key fast amino acid excitatory and inhibitory neurotransmitters in the central nervous system. Impaired glutamate and GABA transport/homeostasis contribute to neuronal dysfunction and pathogenesis of main neurological disorders. One of the crucial processes responsible for proper synaptic neurotransmission is exocytosis, fusion upon stimulation of synaptic vesicles containing neurotransmitter with the plasma membrane of the presynaptic nerve terminals. The Na^+-dependent glutamate and GABA transporters are key players in the termination of synaptic neurotransmission and mediate neurotransmitter uptake to the cytoplasm and establishment of the extracellular level of neurotransmitters. These transporters use Na^+/K^+ electrochemical gradient across the plasma membrane as a driving force. Synaptic vesicles are the acidic compartments of the nerve terminals and accumulate neurotransmitters from the cytosol due to functioning of specific vesicular neurotransmitter transporters driving by the proton electrochemical gradient $\Delta\mu H^+$ generated by V-ATPase that pumps protons into the vesicle interior.

Molecular dynamics simulations, planar phospholipid bilayer membranes (BLMs) and FTIR spectroscopy were used to study interaction of remdesivir with the model cellular and artificial planar membranes and nerve terminals in vitro, respectively. The following parameters were studied in nerve terminals during remdesivir administration in vitro: (1) exocytotic release of the radiolabeled neurotransmitters [^{3}H] GABA and L-[^{14}C] glutamate; (2) the extracellular levels of these neurotransmitters, and tonic leakage of [^{3}H] GABA; (3) transporter-mediated neurotransmitter uptake; (4) transporter-mediated release of the neurotransmitters from nerve terminals stimulated by the membrane depolarization and dissipation of the vesicular proton gradient; and (5) acidification of synaptic vesicles using pH-sensitive fluorescent dye acridine orange (Scheme 1).

2. Methods and materials

2.1. Molecular dynamics simulations

The topology of remdesivir was generated with CHARMM GUI ligand builder [12,13]. The molecule was optimized on 6-31G level of theory using NWChem 6.6 software [14]. The ESP partial charges were computed, averaged for topologically equivalent atoms and applied to generated topology.

The model membrane was generated previously with the lipid composition close to one of the plasma membrane of human lung epithelial cells. We are aware that this composition could be different from synaptosomes, thus obtained results should be interpreted on qualitative level only. We used the average abundance of the lipid head groups from [15,16] and the distribution of the lipid tails inside each lipid class from [17]. Only lipid tails with more than 5% abundance were taken into account. Asymmetry of the lipid content of monolayers was set by putting all PC, SM and ceramide lipids to the outer leaflet and all PE, PS, PI and plasmalogen lipids to the inner leaflet. Cholesterol was distributed equally between the leaflets.

CHARMM GUI membrane builder [12,13] with the lipid composition detailed in Table 1 was used to compose the membrane patch containing

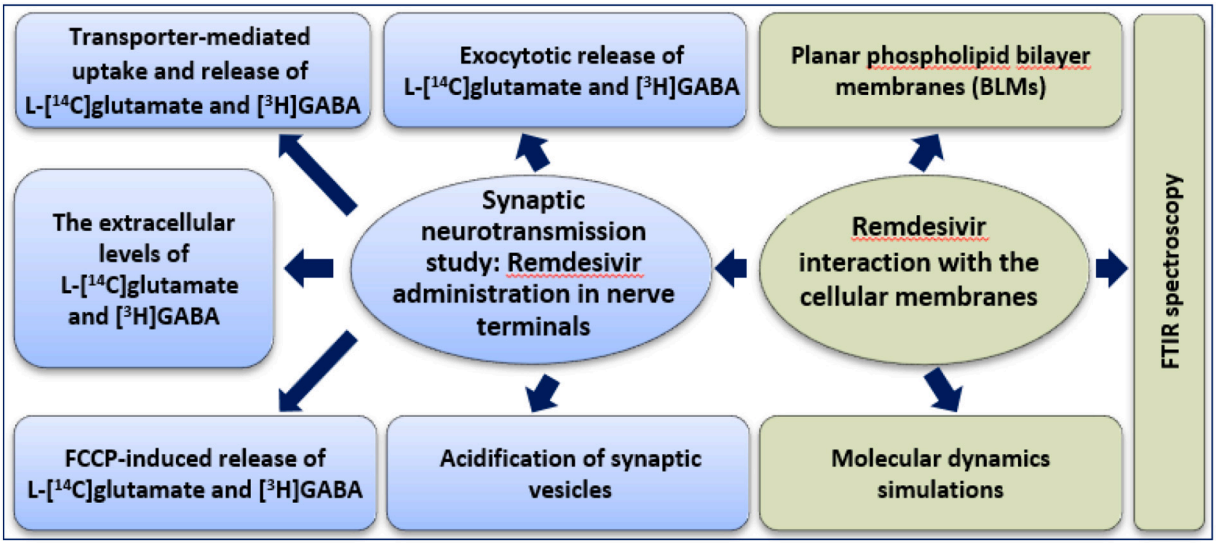

Scheme 1. An experimental roadmap

Table 1
Lipid composition of the model bilayer adjusted to 64 lipids per leaflet. The lipid names correspond to CHARMM GUI naming convention.

Lipid	Outer leaflet	Inner leaflet
DPPC	5	
PLPC	3	
POPC	11	
DOPC	6	
SOPC	4	
SAPC	3	
POPI		4
SAPI		6
DOPE		4
SOPE		5
PLA20		15
SAPE		8
SOPS		7
DOPS		1
SAPS		3
PSM	11	
CER160	7	
CER180	2	
CER241	1	
CHOL	11	11

64 lipids in each monolayer. The membrane was duplicated in X direction to create an elongated membrane patch containing 384 lipids. The system was solvated by ~40,000 water molecules. The number of ions corresponds to 0.15 M of NaCl with additional counter ions added to neutralize the system. Additional slabs of water were added in X direction to convert the system into the bicelle, which is periodic in Y direction. The advantage of the bicelle setup is the absence of the lateral strain caused by uncompensated difference in the areas per lipid in inner and outer leaflets. The bicelle caps serve as reservoirs which accumulate excessive lipids from one monolayer and donate them to the other. As a result both monolayers possess an optimal number of lipids, which changes dynamically during the simulation. The mixing of lipids from different monolayers in the bicelle caps was prevented by means of selective repulsive potentials as described elsewhere [18–23]. The flat form of the bicelle was maintained by means of EnCurv technique [24] with enforced zero curvature. The bicelle was equilibrated for 200 ns.

Three remdesivir molecules were added to equilibrated system directly above the outer leaflet. The centers of masses of remdesivir molecules were kept close to the membrane by means of flat-bottom restraining potential which turns on at 2.5 nm from the membrane center in Z direction. Another flat-bottom potential acting along X axis prevented remdesivir molecules from diffusing into the bicelle caps. The system was simulated for 200 ns.

All simulations were performed in Gromacs [25] versions 2019.2 and 2020.4 patched with Plumed [26,27] with EnCurv extension [24]. The CHARMM36 force field [28] was used. The pressure of 1 atm was maintained by Parrinello-Rahman barostat [29]. Anisotropic pressure coupling was applied along Y direction only (see [23,30]) for the rationale of this choice. The Verlet cutoff scheme was used [31]. The force-switch cut-off of the Van der Waals interactions was used in the region between 1.0 and 1.2 nm. Long range electrostatics was computed with the PME method [32] with the cut-off of explicit short-range electrostatic interactions at 1.2 nm. Velocity rescale thermostat [33] was used at the temperature of 320 K. An integration step of 2 fs was used in all simulations with the bonds to hydrogen atoms converted to rigid constraints. Trajectories were analyzed by a custom script based on Pteros molecular modeling library [34,35]. VMD 1.9.3 [36] was used for visualization.

2.2. Lipid bilayer formation, transmembrane current recordings and data analysis

The pore-formation was assessed by constant monitoring of transmembrane current across suspended planar phospholipid bilayer membranes (BLMs). BLMs were formed by [37] from the solution of cholesterol and zwitterionic phospholipid egg PC in n-heptane. The weight ratio of the egg PC/cholesterol mixtures was maintained at 1:2 with the total lipid concentration of every membrane-forming mixture of 20 mg/ml. Lipid bilayers were suspended in a round aperture of a Delrin cup (0.15 mm diameter, Warner Instruments, Inc., USA) with a working volume of 1 ml. The actual bilayer formation was monitored in reflected light by MBS-9 binocular microscope (St. Petersburg Optico–Mechanical Plant LOMO, Russian Federation) and rectangular test pulses internally generated by BBA-02 amplifier (Eastern Scientific, LLC, Rockville, USA) connected to membrane washing saline through a HS-2 head-stage (Eastern Scientific, LLC, Rockville, USA). The membrane washing solution contained 10 mM Tris–HCl (pH 7.4) and 10 mM or 100 mM KCl. Both membrane separated chambers could be stirred when required.

Voltage-clamp recordings of transmembrane current were made via a high-resolution amplifier BBA-02 (Eastern Scientific, LLC, Rockville, USA). The potential difference was referenced to the outer glass chamber, which was defined as being at ground potential. Voltage was applied to the saline inside Delrin cup held within a glass chamber. Membrane separated saline was connected to HS-2 head-stage of the amplifier BBA-02 through a pair of agar bridges immersed into a 2 M KCl solution with silver chloride electrodes EAG-02 (Eastern Scientific, LLC, Rockville, USA) placed on the opposite sides of suspended bilayer. The polarization between assembled electrodes was maintained at ±1.5 mV. Holding potentials within the range of ±100 mV were applied by universal signal generator RG-3 (Eastern Scientific, LLC, Rockville, USA) or voltage-source built in amplifier BBA-02. Transmembrane currents were filtered at 0.1 kHz and recorded by a computer through USB Digitizer Model ADA-1210 (Eastern Scientific, LLC, Rockville, USA) using Cole-Palmer Instrument Company software (Illinois, USA). The computer-made records were analyzed with Origin Pro 8.6.0 software. All experiments were carried out at a room temperature (20–24 °C), each made on freshly suspended membrane.

2.3. Ethical approval

Animals (Wistar rats, males, body weight of approx. 120 g) were kept in the animal facilities of the Palladin Institute of Biochemistry NAS of Ukraine, housed in a temperature-controlled room (22–23 °C), and provided ad libitum with water and dry food pellets. The animal experiments were performed in accordance with the Guidelines of the European Community (2010/63/EU) and local laws/policies, and were approved by the Animal Care and Use Committee of the Palladin Institute of Biochemistry NAS of Ukraine (Protocol from September 21, 2020). All animal studies were reported in accordance to the ARRIVE guidelines for reporting experiments involving animals [38,39]. The total number of rats used in the study was 36, specifically, the measurements of the extracellular levels and uptake of L-[^{14}C] glutamate and [^{3}H] GABA in nerve terminals – 12 animals; release of L-[^{14}C] glutamate and [^{3}H] GABA – 12 animals; fluorimetry – 12 animals.

2.4. Isolation of nerve terminals (synaptosomes) from the cortex regions of the rat brains

The cortex brain region isolated from decapitated rats was rapidly removed, and then homogenized in the ice-cold solution containing 0.32 M sucrose, 5 mM HEPES-NaOH, pH 7.4, and 0.2 mM EDTA. One synaptosome preparation was obtained from one rat, and each measurement was done in triplicate. The synaptosome preparations were obtained using differential and Ficoll-400 density gradient centrifugations of rat brain homogenate according to [40–42]. The synaptosome preparations were used in the experiments during 2–4 h. The standard salt solution contained (in mM): NaCl 126; KCl 5; $MgCl_2$ 2.0; NaH_2PO_4 1.0; HEPES 20, pH 7.4; and D-glucose 10. Ca^{2+}-containing media were

supplemented with 2 mM $CaCl_2$. Ca^{2+}-free media were supplemented with 2 mM EGTA. Protein concentration was examined according to [43].

2.5. FTIR spectroscopy

Synaptosomes without remdesivir and after incubation with remdesivir (0.028 mg/ml) were analyzed using INVENIO-R instrument (Bruker, Germany). Two types of preparations of synaptosomes of different functional states were used in FTIR experiments. The first one was functionally active synaptosomes with normal membrane potential, which were characterized by a high capability to accumulate potential-sensitive fluorescent dye rhodamine 6 G. The accumulation level was 0.2 a.u., calculated as $F = F_t/F_0$, where F_0 and F_t were fluorescence intensities of rhodamine 6 G in the absence and presence of the synaptosomes, respectively. The second one was functionally inert synaptosomes, which were kept in freezer under −24 °C during few weeks. They were characterized by a low capability to accumulate rhodamine 6 G. The accumulation level was less than 0.95 a.u. (no membrane potential), calculated according to above equation.

To register the FTIR-ATR spectra, 20 μl of the synaptosome suspension was applied to ZnSe crystal of the Bio-ATR attachment. The sample was dried in the spectrometer sample compartment for 1 h in a stream of nitrogen at room temperature fixing a state of synaptosomes at the present moment. The spectra were registered until the OH band at 3400 cm^{-1} stopped changing and the sample was dried. For FTIR-ATR spectra, the baseline correction and band intensity normalization by the Amide *I* band centered at 1652 cm^{-1} have been done on the basis of supposition that a number of protein molecules was constant in the synaptosomes of both functional states.

2.6. The exocytotic and transporter-mediated release and the extracellular level of L-[^{14}C] glutamate in the nerve terminal preparations

The synaptosome preparations were diluted in the standard salt solution to reach a concentration of 2 mg of protein/ml, and after pre-incubation at 37 °C for 10 min were loaded with L-[^{14}C] glutamate (2.81 μM, 1 μCi/ml) in the standard salt solution at 37 °C for 10 min. After loading procedure, the synaptosome suspensions were washed with 10 volumes of ice-cold standard salt solution; the pellets were re-suspended in the standard salt solution to reach a final concentration of 1 mg of protein/ml. Synaptosome suspensions (125 μl; 0.5 mg of protein/ml) were pre-incubated at 37 °C for 10 min, then aliquots of remdesivir stock solution in dimethyl sulfoxide (DMSO) were added and incubated with synaptosomes for 10 min, and then sedimented using a microcentrifuge (20 s at 10,000*g*). Control synaptosome samples contained DMSO in related concentrations. The extracellular level of L-[^{14}C] glutamate in the nerve terminal preparations was measured in Ca^{2+}-free media. The transporter-mediated release of L-[^{14}C] glutamate from synaptosomes was stimulated by 35 mM KCl or the protonophore FCCP in Ca^{2+}-free media, and measured for 6 min. The exocytotic release of L-[^{14}C] glutamate from synaptosomes, stimulated by membrane depolarization with 35 mM KCl, was measured at 6 min time point and calculated by subtraction of the L-[^{14}C] glutamate release values in Ca^{2+}-containing media from those in Ca^{2+}-free one. The extracellular level and release of L-[^{14}C] glutamate were recorded in the aliquots of supernatants (100 μl) and pellets using liquid scintillation counting with Sigma-Fluor® High Performance LSC Cocktail (1.5 ml), and the values were expressed as the percentage of total accumulated synaptosome L-[^{14}C] glutamate [44,45]. L-[^{14}C] glutamate release data were collected in triplicate from several (n) independent experiments performed with different synaptosome preparations.

2.7. The exocytotic, transporter-mediated, and tonic release and the extracellular level of [^{3}H] GABA in the nerve terminal preparations

The synaptosome preparations were diluted in the standard salt solution up to 2 mg of protein/ml, and after their pre-incubation at 37 °C for 10 min were loaded with [^{3}H] GABA (50 nM, 4.7 μCi/ml) in the standard salt solution for 10 min. GABA transaminase inhibitor aminooxyacetic acid at a concentration of 100 μM was used in the experiments of [^{3}H] GABA loading and release to minimize the formation of GABA metabolites. After loading, the synaptosome suspensions were washed with 10 volumes of ice-cold standard salt solution. The pellets were re-suspended in the standard salt solution to have protein concentration of 1 mg of protein/ml. Synaptosome suspensions (120 μl) were pre-incubated at 37 °C for 10 min, then the aliquots of remdesivir stock solution in DMSO were added and incubated for 10 min, and sedimented using a microcentrifuge (20 s at 10,000*g*). Control synaptosome samples contained DMSO in related concentrations. The extracellular level of [^{3}H] GABA in synaptosome preparations was recorded in Ca^{2+}-containing media. Tonic leakage of [^{3}H] GABA from nerve terminals was recorded during simultaneous blockage of GABA transporters by NO-711 (30 μM), and expressed as elevated by NO-711 extracellular level of [^{3}H] GABA. The exocytotic release of [^{3}H] GABA from nerve terminals was stimulated by 15 mM KCl in Ca^{2+}-containing media in the presence of NO-711 (30 μM) and measured at 5 min time point. The transporter-mediated release of [^{3}H] GABA from synaptosomes was stimulated by 35 mM KCl or protonophore FCCP in Ca^{2+}-free media, and measured for 5 min. [^{3}H] GABA radioactivity was measured in the aliquots of supernatants (90 μl) by liquid scintillation counting with Sigma-Fluor® High Performance LSC Cocktail (1.5 ml), and the values were expressed as the percentage of total accumulated synaptosome [^{3}H] GABA [45–47]. [^{3}H] GABA release data were collected in triplicate from several (n) independent experiments performed with different synaptosome preparations.

2.8. The initial rate and accumulation of L-[^{14}C] glutamate by the nerve terminals

L-[^{14}C] glutamate uptake by synaptosomes was measured as follows. Synaptosome suspensions (125 μl of suspension, 0.4 mg of protein/ml) were pre-incubated in the standard salt solution at 37 °C for 10 min with the remdesivir aliquots in DMSO. The uptake was initiated by the application of L-glutamate and L-[^{14}C] glutamate (10 μM and 450 nM, 0.167 μCi/ml, respectively). The synaptosomes were more incubated at 37 °C for 1 min (the initial rate value) and 10 min (the accumulation value), and then sedimented using a microcentrifuge (20 s at 10,000 ×*g*). Control synaptosome samples contained DMSO in related concentrations. Nonspecific binding of L-[^{14}C] glutamate was assessed in cooled samples after the adding of radioactivity. L-[^{14}C] glutamate uptake was measured based on a decrease in radioactivity in the aliquots of supernatants (100 μl) and an increase in radioactivity in SDS-treated pellets. L-[^{14}C] glutamate uptake was calculated using liquid scintillation counting with Sigma-Fluor® High Performance LSC Cocktail (1.5 ml) [48]. L-[^{14}C] glutamate uptake data were collected in triplicate from several (n) independent experiments performed with different synaptosome preparations.

2.9. The initial rate and accumulation of [^{3}H] GABA by the nerve terminals

Synaptosomes were diluted by the standard salt solution containing aminooxyacetic acid (100 μM). The protein concentration in the synaptosome samples was 200 μg/ml. The synaptosome preparations were pre-incubated at 37 °C for 10 min, the remdesivir aliquots in DMSO were added to the synaptosome suspensions, and the samples were further incubated for 10 min. Control synaptosome samples contained DMSO in related concentrations. The uptake was initiated by the addition of

GABA and [^{3}H] GABA (1 μM or 50 nM, 4.7 μCi/ml, respectively). To determine the initial rate of [^{3}H] GABA uptake, this process was completed in 1 min by filtering aliquots through Whatman GF/C filters. After washing twice with 5 ml of ice-cold standard salt solution, the filters were dried, and then were suspended in the organic counting scintillant and counted using a scintillation counter. Nonspecific binding of [^{3}H] GABA was evaluated in cooled samples filtered immediately after the adding of radioactivity [49]. [^{3}H] GABA uptake data were collected in triplicate from several (n) independent experiments performed with different synaptosome preparations.

2.10. Measurements of synaptic vesicle acidification in the nerve terminals

Acridine orange, a pH-sensitive fluorescent dye, was selectively accumulated by the acid compartments of nerve terminals, namely synaptic vesicles [50]. The changes in the dye fluorescence were measured using spectrofluorometer PTI QuantaMaster40 and Hitachi at excitation and emission wavelengths of 490 and 530 nm, respectively. The reaction was started by the application of acridine orange (a final concentration of 5 μM) to synaptosome suspensions (0.2 mg/ml of final protein concentration) pre-incubated in a stirred thermostated cuvette at 37 °C for 10 min. Fluorescence (F) was calculated according to: $F = F_t/F_0$, where F_0 and F_t were fluorescence intensities of the dye in the absence and presence of the synaptosomes, respectively. F_0 was calculated by extrapolation of exponential decay function to $t = 0$.

2.11. Materials

EGTA, EDTA, HEPES, Ficoll 400, DMSO, Whatman GF/C filters, NO-711, FCCP, Sigma-Fluor® High Performance LSC Cocktail, the analytical grade salts were purchased from Sigma (USA); remdesivir were from Tocris Bioscience (Bristol, UK); L-[^{14}C] glutamate and [^{3}H] GABA (γ-[2,3-3H(N)]-aminobutyric acid) were from Perkin Elmer (Waltham, MA, USA). Acridine orange and rhodamine 6G were obtained from Molecular Probes (USA).

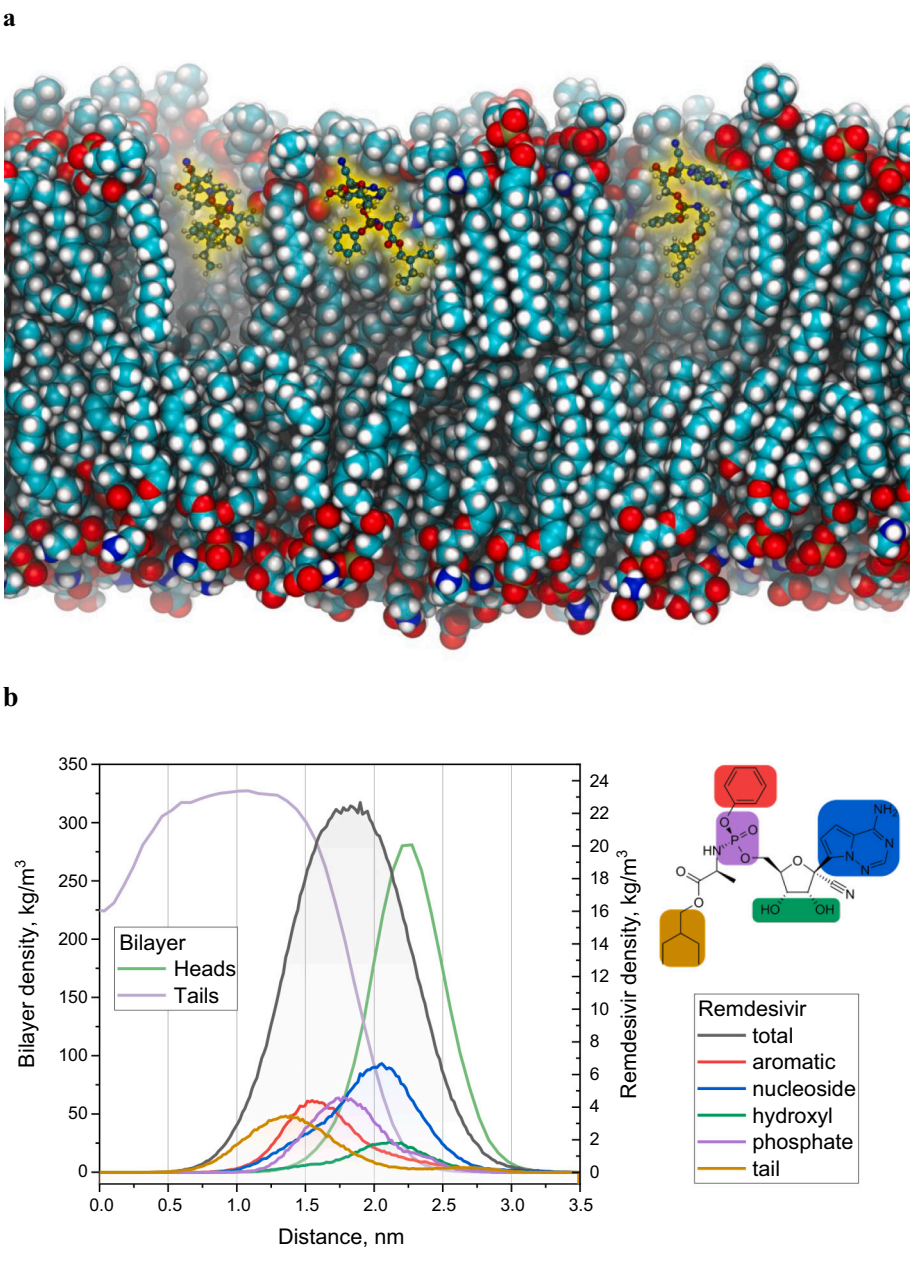

Fig. 1. Remdesivir amphiphilicity study.
a – Position and orientation of remdesivir in the model membrane. Snapshot from MD trajectory at 200 ns. Lipids are shown in space-fill representation while remdesivir molecules are rendered as balls and sticks and highlighted for clarity. The lipids, which obscure the remdesivir molecules are removed. The picture shows the central bilayer region of the simulated bicelle used for analysis. b – Density distributions of the lipid head groups and tails (left axis) and different chemical groups of remdesivir (right axis). The colors of selected chemical groups in remdesivir molecule (top right) correspond to the colors of the curved. Only the outer membrane leaflet is shown.

2.12. Statistical analysis

The experimental data were expressed as the mean ± S.E.M. of n independent experiments. The difference between two groups was compared by one-way ANOVA. Differences were considered significant, when $p < 0.05$.

3. Results

3.1. Molecular dynamics simulations

Remdesivir molecules incorporate spontaneously into the membrane during first 10–20 ns and remain intercalated between the lipids of the outer leaflet during the whole simulation. Visual inspection shows no signs of aggregation or dimerization of remdesivir molecules despite its active lateral diffusion. Typical positions and orientations of REM molecules in the model membrane are shown in Fig. 1a.

Fig. 1b shows density distributions of the lipid head groups and tails and different remdesivir chemical groups. It is evident that the most hydrophilic moieties of remdesivir (hydroxyl groups and nucleoside) are oriented towards the aqueous solution and located at the level of lipid head groups. In contrast, the most hydrophobic moieties (the aromatic ring and the branched hydrocarbon tail) are located at the level of lipid tails in the hydrophobic core of bilayer. The phosphate moiety is located at the interface of lipid head groups and tails.

In general, remdesivir sits rather deep in the bilayer, on average ~1.7 nm from its center. It is subject to substantial normal and lateral diffusive motions in the course of simulations but it never detaches from bilayer or changes its preferred orientation.

Although the simulations were performed for complex lipid mixture mimicking the composition of the cellular membranes of lung epithelial cells, no specific interactions of remdesivir with particular lipid species were observed. Spontaneous incorporation or remdesivir molecules occurs randomly in respect to exposed lipids and is driven by the minimization of hydrophobic mismatch of its aliphatic moieties and favourable interaction of the polar moieties with the lipid head groups and water. This suggests that the same thermodynamic mechanism, which is similar for the majority of amphiphilic membranotropic compounds, also drives incorporation of remdesivir into the simpler model membranes containing only few lipid species.

Our simulations do not allow studying specific influence of lipid unsaturation, polarity and charge on the incorporation of remdesivir. In order to get such information, the series of simulations with different lipid compositions should be performed, which is beyond the scope of this study.

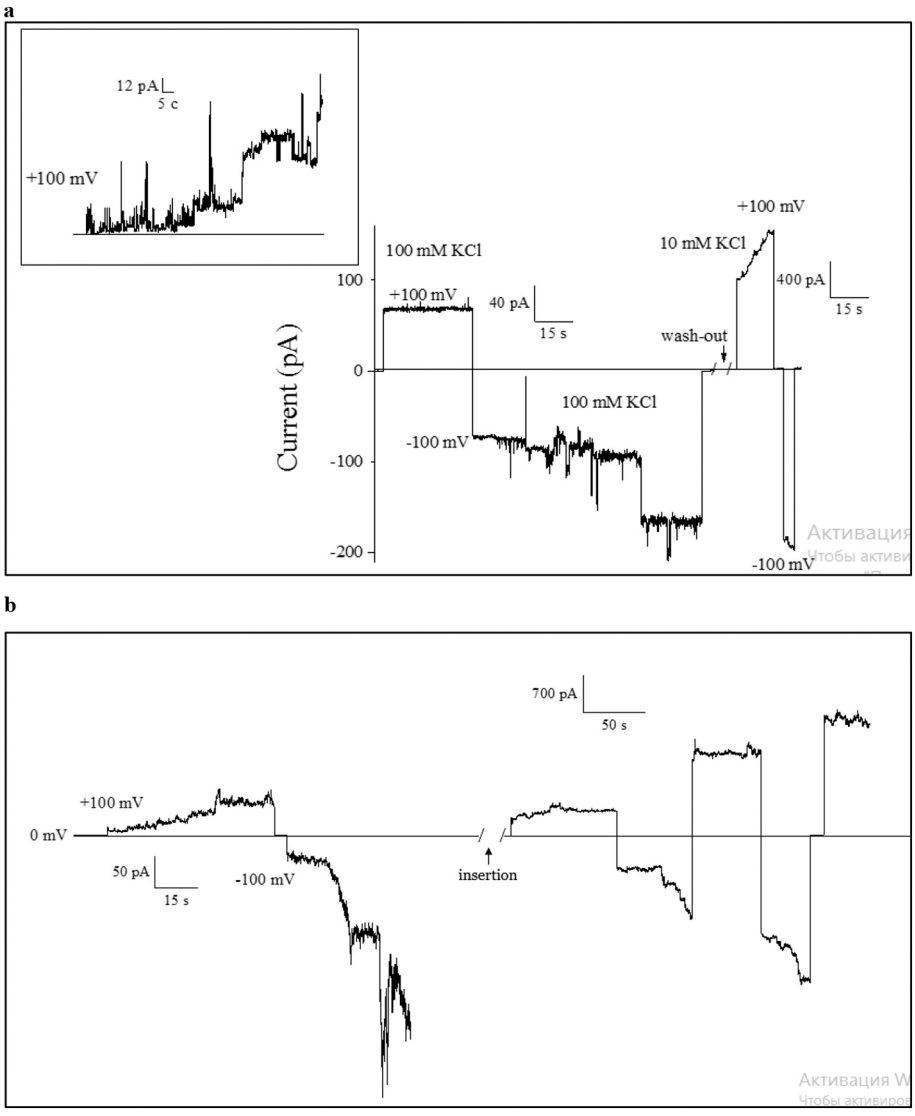

Fig. 2. a – Current-time traces induced by the interaction of remdesivir with egg PC/cholesterol suspended planar bilayers (weight ratio of 2:1) and remdesivir-induced single pore conductances. Remdesivir was added to a final concentration of 100 μM. Membrane separated solution contained 100 mM KCl (pH 7.4). Currents were monitored under +100 mV (resulting current is shown above zero line) and −100 mV (resulting current is shown below zero line) applied on the side of BLM opposite to where the drug was introduced. Remdesivir-induced pore openings are shown as downward deflections observed at a holding potential of −100 mV. Solid line represents zero current. To diminish the effect of membrane capacity, a little extra time (1–2 s) was allowed before recording after application of each consecutive voltage pulse. To determine the selectivity of remdesivir-induced current, the symmetrical membrane-bathing solution of 100 mM KCl (pH 7.4) was then changed in the cis chamber (drug-addition side) for 10 mM KCl (pH 7.4). The record was paused for the time of washout and resumed later to monitor the shift of zero current potential. Inset: Remdesivir-induced pore openings are shown as upward deflections observed at a holding potential of +100 mV in symmetrical solution of 100 mM KCl (pH 7.4). Solid line represents zero current.
b – Current-time traces exhibiting dependence of the insertion of remdesivir into egg PC/cholesterol suspended planar bilayers (weight ratio of 2:1) upon the sign of membrane potential.

3.2. Conductivity of the BLMs after remdesivir administration

3.2.1. Pore-formation induced by remdesivir in cholesterol-containing BLMs

The introduction of remdesivir at a concentration of 100 μM to PC/cholesterol BLM kept at 2:1 weight ratio was followed by the appearance of step-like increases in transmembrane current indicative of pore-formation (Fig. 2a). This included relatively stable increases in current and those interrupted by brief falls within a fluctuating diameter of each separate step, which suggest rapid resealing of the single pore (Fig. 2a). The mean unitary conductance of stable single-pore events varied in magnitude within the range of ~10 pS to ~360 pS at a holding potential of 100 mV (Fig. 2a, insert). Similar distribution of stable single-pore conductance events was also represented by amplitudes obtained at a negative voltage, −100 mV applied to the same side of membrane except for the appearance of larger increases in current (Fig. 2a).

The pore-formation occurred in the symmetrical membrane washing water solution of 100 mM KCl at 100 mV voltage applied on the side of membrane to which remdesivir was added, regardless to the sign of the membrane potential (Fig. 2a). This suggests that the sign of membrane potential is not the necessary prerequisites for remdesivir-induced pore-formation. It should be noted that positive holding potential (+100 mV) applied to drug-containing side of membrane decreased the lag-time preceding the creation of transmembrane ion-conductive pores and increased the rate of insertion as compared to negative holding potential (−100 mV) (Fig. 2a, b). Remdesivir-induced pore-formation facilitated by positive potential applied on the drug-addition side can be consistent with physiological situation where the positive sign of resting potential outside of susceptible cell activates membrane insertion of remdesivir molecules due to the presence of multiple positively charged nitrogen-containing groups.

Increasing amount of stable, lack in complete resealing pores eventually formed a temporary quasi steady-state integral current consisting of many remdesivir pores (Fig. 2b). Conversely, lasting remdesivir-induced increase in current could be partially stabilized by flushing drug-containing compartment with drug-free saline. This suggests mostly irreversible binding of remdesivir with sterol-containing almost neutral phospholipid bilayer.

3.2.2. Potential-dependence and ionic selectivity of remdesivir pores

The effect of applied voltage gradients on magnitude of single pore conductance and a steady-state current flowing across remdesivir-modified bilayer was explored by switching holding potentials between ±100 mV (Fig. 2a, b). The steady-state macroscopic current induced by the drug in cholesterol-containing phospholipid bilayer exhibited almost no dependence upon the sign of the membrane potential with a rectification asymmetry coefficient of 0.9 (Fig. 2a). Linear current-voltage dependence at positive and negative voltages applied to the side opposite to which remdesivir was added also implies that at 2-times lower holding potential (±50 mV), the single pore conductance and summary current will be reduced approximately by a factor of 2 for the type of BLMs tested.

The Nernst potential obtained for summary remdesivir-induced current in the membrane washing saline of 10 mM KCl on addition side and 100 mM KCl on the opposite side of PC/cholesterol membrane consisted of 0 mV (Fig. 2a). This suggests the lack in cation/anion selectivity of remdesivir-created summary current [51]. Nearly 1 asymmetry coefficient and the absence of ionic selectivity determined for stationary macroscopic remdesivir-induced current suggested no sufficient prevalence of inward current over outward current of the ions across drug-induced pores in plasma membranes of susceptible cells at positive potentials applied to the addition side that corresponded to the physiological situation, where remdesivir pores are formed on extracellular side.

Therefore, the application of positive potential (+100 mV) to the remdesivir - addition side facilitated the insertion of remdesivir into the membrane washed in symmetrical solution of 100 mM KCl (pH 7.4) as compared with negative potential (−100 mV) and smaller positive and negative potentials (+50 mV and −50 mV). Remdesivir pores exhibited a wide range distribution of conductances between ~10 pS and 650 pS, which suggests the clustering of the smallest repeatable ion-conductive structures (~10 pS) and/or the presence of much larger particles also capable of pore-formation. Lack in cation/anion selectivity and appreciable rectification of summary remdesivir-induced steady-state currents at positive and negative voltages suggests approximately equal contribution of the inward and outward ionic currents across the target-cell plasma membrane at the physiological situation, where the drug is present on the extracellular side.

3.3. FTIR spectroscopy of nerve terminals after remdesivir administration

Interaction of remdesivir with synaptosomes was examined using FTIR-ATR spectroscopy. Two types of preparations of synaptosomes of different functional states were used in the experiments, i.e. the functionally active and functionally inert synaptosomes (see Method section). An increase in the intensity of the Amide A band was recorded after remdesivir action on functionally active synaptosomes, apparently due to an increase in the contribution of OH-NH stretching vibrations (Fig. 3a). In the area of absorption of the Amide *I* and Amide II bands, the changes were insignificant. The Amide I band has a characteristic position for the dominant contribution of the α-conformation of proteins at 1650 cm^{-1} with band asymmetry at 1628 cm^{-1} (contribution of β-layers). Similarly, the region of 1500–1300 cm^{-1} was without changes, where the absorption bands of the deformation vibrations of CH can be registered. However, the changes were observed in the area of absorption of phosphate groups PO_2^-, namely the appearance of the shoulder at 1208 cm^{-1} in the bands of asymmetric stretching bands PO_2^- (1226 cm^{-1}) in the synaptosome sample after incubation with remdesivir. There was also an increase in the intensity of the bands at 1135 and 1049 cm^{-1}, as well as at 988 and 926 cm^{-1}. Therefore, the changes in hydrogen binding in hydrogen-bound groups, and especially in phosphate groups were attributed to functionally active synaptosomes during their interaction with remdesivir. The nature of spectral differences was not in frequency shifts, but in changes in the contribution of bands to intensity.

Functionally inert synaptosomes (Fig. 3b) showed different changes after remdesivir administration as compared to the functionally active ones (Fig. 3a). After interaction with remdesivir, high-frequency shift of the PO_2-*asym* band from 1232 to 1236 cm^{-1}, an increase in contribution of 1146 cm^{-1}, and in addition, low-frequency shift of the CO band from 982 to 976 cm^{-1} and low-frequency C═O shift from 1740 to 1736 cm^{-1} were registered. In contrast to experiments with functionally active synaptosomes, here it was registered an increase in the contribution of CH stretching vibrations in the region of 3000–2800 cm^{-1}. There was also an increase in the contribution of deformations of CH at 1399 cm^{-1}. An increase in the intensity of vibrations of other functional groups indicated that the bonds in the system have become weaker. The integral intensity of the difference spectrum in the region of 3800–630 cm^{-1} was equal to 16.8 for functionally active synaptosomes (Fig. 3a, black bottom line) and 26.2 – for functionally inert synaptosomes (Fig. 3b, black bottom line). It can be concluded that the drug undoubtedly affected the membrane of synaptosomes, although this effect was quite insignificant in terms of spectroscopic features.

3.4. Radiolabel assay

Beside specific barrier function of the plasma membranes in the majority of cells, the plasma membrane of nerve cells is directly involved in realization of their functional activity, i.e. signal transduction. Taking into account membranotropic action of remdesivir (Figs. 1–3), its effects on key characteristics of synaptic neurotransmission were analyzed in nerve terminals using radiolabelled and fluorescence assays.

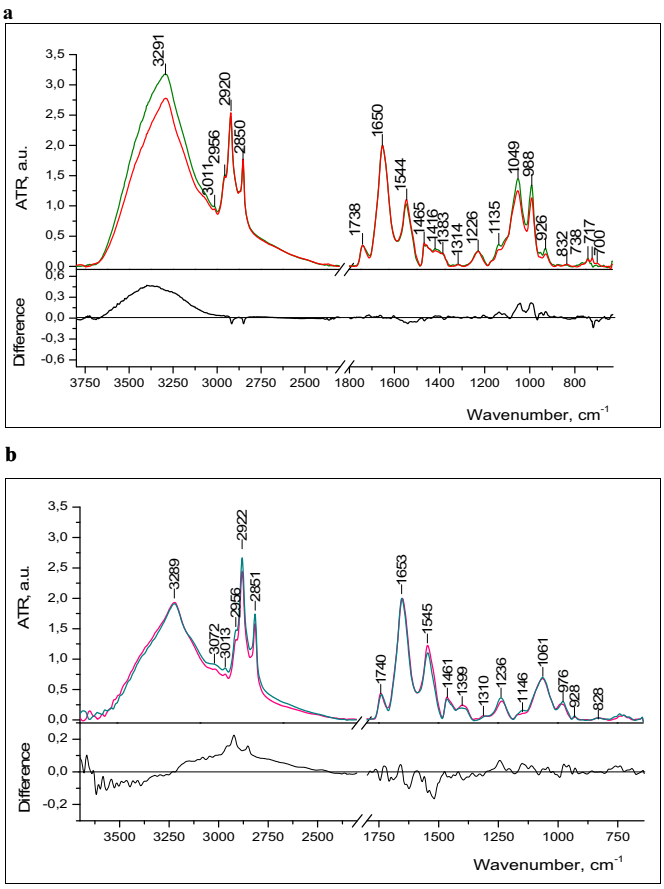

Fig. 3. FTIR-ATR spectra of functionally active (a) and functionally inert (b) synaptosomes in the control (without remdesivir) (a, b - red lines) and in the presence of remdesivir (a, b - green lines). a, b (black bottom lines) – difference in the synaptosome spectra (obtained by subtraction of the synaptosome spectra after incubation with remdesivir from the spectra of control synaptosomes without remdesivir). Functionally active synaptosomes were incubated at 37 °C for 5 min to restore their ion gradients [44]. To register the FTIR-ATR spectra, 20 μl of the synaptosome suspension was applied to the ZnSe crystal of the Bio-ATR attachment. After that the sample was dried in the spectrometer sample compartment for 1 h in a stream of nitrogen. The spectra were registered until the OH band at 3400 cm^{-1} stopped changing and the sample was dried. After recording the spectra, the baseline was corrected and the absorption spectra were normalized.

3.4.1. Exocytotic release of L-[^{14}C]glutamate and [^{3}H]GABA from nerve terminals during remdesivir administration

KCl (35 mM) - induced Ca^{2+}-dependent exocytotic release of L-[^{14}C] glutamate from nerve terminals was decreased by remdesivir in a dose-dependent manner (Fig. 4a). The exocytotic release value was 6.25 ± 0.44% of total synaptosome label in the control, 4.98 ± 0.43% of total synaptosome label in presence of remdesivir at a concentration of 1 μM [$F_{(1,22)} = 4.67$; $p < 0.05$; $n = 12$], 2.80 ± 0.47% of total synaptosome label in presence of remdesivir at a concentration of 10 μM [$F_{(1,22)} = 18.02$; $p < 0.001$; $n = 12$], 0.70 ± 0.17% of total synaptosome label in presence of remdesivir at a concentration of 100 μM [$F_{(1,22)} = 63.49$; $p < 0.001$; $n = 12$].

Ca^{2+}- dependent exocytotic release of [^{3}H]GABA from nerve terminals was stimulated by KCl (15 mM) and measured during blockage of transporter-mediated GABA uptake by NO-711 (30 μM). 1 μM remdesivir did not change the exocytotic release of [^{3}H]GABA from nerve terminals, whereas 10 μM remdesivir and higher decreased the release value. As shown in Fig. 4b, the release was 8.36 ± 0.61% of total synaptosome label in the control, 7.48 ± 0.63% of total synaptosome label in the presence of remdesivir at a concentration of 1 μM [$F_{(1,22)} = 1.14$; $p = 0.3$; n = 12], 5.69 ± 0.53% of total synaptosome label in the presence of remdesivir at a concentration of 10 μM [$F_{(1,22)} = 11.91$; $p < 0.01$; $n = 12$], and 4.52 ± 0.41% of total synaptosome label in the presence of remdesivir at a concentration of 100 μM [$F_{(1,22)} = 29.65$; $p < 0.001$; $n = 12$].

Therefore, remdesivir at a concentration of 1 μM had no significant effect on the exocytotic release of [^{3}H]GABA, but influenced that of L-[^{14}C]glutamate in nerve terminals. An increase in drug concentrations up to 10 and 100 μM caused a significant dose-dependent decrease in this parameter for both neurotransmitters.

3.4.2. The extracellular levels of L-[^{14}C]glutamate and [^{3}H]GABA, and tonic leakage of [^{3}H]GABA from nerve terminals during remdesivir administration

As shown in Fig. 4c, the extracellular level of L-[^{14}C]glutamate was not changed by remdesivir at concentrations of 1, 10, 100 μM that was equal to 18.48 ± 0.83% of total synaptosome label in the control, 18.51 ± 0.52% of total synaptosome label in presence of remdesivir at a concentration of 1 μM [$F_{(1,22)} = 0.001$; $p = 0.97$; $n = 12$], 18.79 ± 0.58% of total synaptosome label in presence of remdesivir at a concentration of 10 μM [$F_{(1,22)} = 0.1$; $p = 0.75$; n = 12], 19.62 ± 1.13% of total synaptosome label in presence of remdesivir at a concentration of 100 μM [$F_{(1,22)} = 0.69$; $p = 0.41$; $n = 12$].

As shown in Fig. 4d, the extracellular level of [^{3}H]GABA was 13.25 ± 0.37% of total synaptosome label in the control, 11.76 ± 0.42% of total synaptosome label in the presence of remdesivir at a concentration of 1 μM [$F_{(1,22)} = 7.62$; $p < 0.05$; $n = 12$], 11.09 ± 0.35% of total synaptosome label in the presence of remdesivir at a concentration of 10 μM [$F_{(1,22)} = 19.52$; $p < 0.001$; $n = 12$], 10.01 ± 0.33% of total synaptosome label in the presence of remdesivir at a concentration of 100 μM [$F_{(1,22)} = 46.45$; $p < 0.001$; $n = 12$].

Tonic leakage of [^{3}H]GABA from nerve terminals was recorded during simultaneous blockage of GABA transporters by NO-711 (30 μM), and expressed as the extracellular level of [^{3}H]GABA elevated by this blocker. No changes in tonic [^{3}H]GABA leakage between the control and synaptosomes in the presence of remdesivir at concentrations of 1, 10, 100 μM were shown (Fig. 4e). Elevated by NO-711 extracellular level of [^{3}H]GABA in synaptosome preparations was 25.18 ± 1.06% of total synaptosome label in the control and 24.93 ± 1.15% of total synaptosome label in presence of remdesivir at a concentration of 1 μM [$F_{(1,22)} = 0.03$; $p = 0.87$; n = 12], 24.85 ± 1.03% of total synaptosome label in presence of remdesivir at a concentration of 10 μM [$F_{(1,22)} = 0.06$; $p = 0.81$; n = 12], 25.29 ± 1.35% of total synaptosome label in presence of remdesivir at a concentration of 100 μM [$F_{(1,22)} = 0.005$; $p = 0.95$; $n = 12$].

Therefore, remdesivir at concentrations of 1, 10, 100 μM did not change the extracellular level of L-[^{14}C] glutamate in nerve terminal preparations, but decreased this level of [^{3}H]GABA. Tonic leakage of [^{3}H]GABA from nerve terminals was not changed, thereby showing absence of remdesivir-induced changes in the membrane permeability for this neurotransmitter.

3.4.3. Transporter-mediated uptake of L-[^{14}C]glutamate and [^{3}H]GABA by nerve terminals during remdesivir administration

As shown in Table 2, remdesivir did not change the initial rate of uptake and accumulation of L-[^{14}C] glutamate for 10 min by nerve terminals.

The initial rate of [^{3}H]GABA uptake by nerve terminals was equal to 164.27 ± 9.54 pmol/min/mg of protein in the control, 159.02 ± 6.79 pmol/min/mg of protein in the presence of remdesivir at a concentration of 1 μM [$F_{(1,22)} = 0.22$; $p = 0.64$; n = 12], 135.50 ± 7.97 pmol/min/mg of protein in the presence of remdesivir at a concentration of 10 μM [$F_{(1,22)} = 5.83$; $p < 0.05$; n = 12], and 121.99 ± 3.01 pmol/min/mg of protein in the presence of remdesivir at a concentration of 100 μM [$F_{(1,22)} = 19.51$; $p < 0.001$; $n = 12$]. Accumulation of [^{3}H] GABA by nerve terminals for 5 min consisted of 563.13 ± 20.92 pmol/mg of

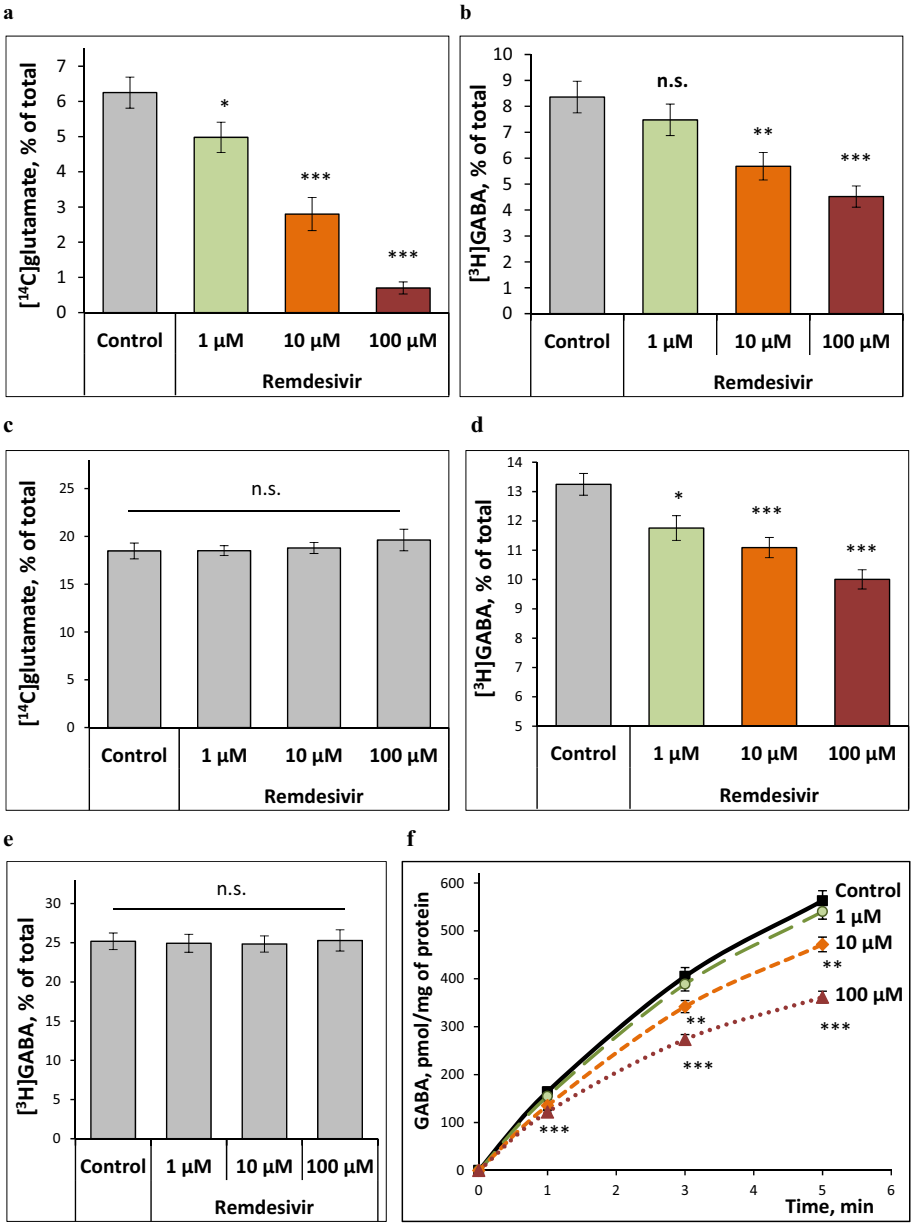

Fig. 4. a, b – Depolarization-induced Ca^{2+}-dependent exocytotic release of L-[^{14}C]glutamate (a) and [^{3}H] GABA (b) from nerve terminals in the control and in the presence of remdesivir at concentrations of 1, 10, 100 μM. Data are the mean ± SEM. n.s., no significant differences; *, $p < 0.05$; **, $p < 0.01$; ***, $p < 0.001$, as compared to the control; $n = 12$.
c, d, e – The extracellular level of L-[^{14}C]glutamate (c) and [^{3}H]GABA (d) in the nerve terminal preparations; tonic leakage of [^{3}H] GABA from nerve terminals during blockage of GABA transporters by NO-711 (30 μM) (e) in the control and in the presence of remdesivir at concentrations of 1, 10, 100 μM. Data are the mean ± SEM. *, $p < 0.05$; ***, $p < 0.001$; n.s., no significant differences as compared to the control; $n = 12$.
f – The initial rate of transporter-mediated uptake and accumulation of [^{3}H]GABA by nerve terminals in the presence of remdesivir at concentrations of 1, 10, 100 μM. Data are the mean ± SEM. **, $p < 0.01$; ***, $p < 0.001$ as compared to the control; $n = 12$.

Table 2
L-[^{14}C] glutamate uptake by nerve terminals in the presence of remdesivir.

	The initial rate of L-[^{14}C] glutamate uptake by nerve terminals (nmol/min/mg of protein)	*p*-Value	Accumulation of L-[^{14}C] glutamate by nerve terminals for 10 min (nmol/mg of protein)	*p*-Value
Control	2.52 ± 0.13		9.97 ± 0.16	
Remdesivir 1 μM	2.84 ± 0.19	$p = 0.15$ n.s.	10.40 ± 0.26	$p = 0.17$ n.s.
Remdesivir 10 μM	2.71 ± 0.12	$p = 0.25$ n.s.	10.43 ± 0.24	$p = 0.12$ n.s.
Remdesivir 100 μM	2.41 ± 0.07	$p = 0.46$ n.s.	9.79 ± 0.09	$p = 0.32$ n.s.

n.s., no significant differences as compared to the appropriate control; $n = 12$.

protein in the control, 540.49 ± 15.84 pmol/mg of protein in the presence of remdesivir at a concentration of 1 μM [$F_{(1,22)} = 0.81$; $p = 0.38$; $n = 12$], 471.84 ± 15.36 pmol/mg of protein in the presence of remdesivir at a concentration of 10 μM [$F_{(1,22)} = 13.50$; $p < 0.01$; $n = 12$] and 361.80 ± 12.24 pmol/mg of protein in the presence of remdesivir at a concentration of 100 μM [$F_{(1,22)} = 75.26$; $p < 0.001$; $n = 12$] (Fig. 4f).

Therefore, remdesivir did not affect L-[^{14}C] glutamate uptake, whereas it decreased [^{3}H] GABA uptake in a dose-dependent manner starting from a concentration of 10 μM, thereby demonstrating diverse effects on uptake of excitatory and inhibitory neurotransmitters.

3.4.4. Depolarization-induced transporter-mediated release of L-[^{14}C] glutamate and [^{3}H] GABA from nerve terminals during remdesivir administration

Remdesivir at concentrations of 1, 10, 100 μM did not influence Ca^{2+}-independent transporter-mediated synaptosomal release of L-[^{14}C] glutamate stimulated by 35 mM KCl that was 7.15 ± 0.83% of total synaptosome label in the control, 7.06 ± 0.7% of total synaptosome

label in the presence of remdesivir at a concentration of 1 μM [$F_{(1,22)} = 0.007$; $p = 0.93$; $n = 12$], 6.86 ± 0.98% of total synaptosome label in the presence of remdesivir at a concentration of 10 μM [$F_{(1,22)} = 0.05$; $p = 0.82$; n = 12], and 7.67 ± 0.93% of total synaptosome label in the presence of remdesivir at a concentration of 100 μM [$F_{(1,22)} = 0.19$; $p = 0.66$; n = 12] (Fig. 5a).

Remdesivir at concentrations of 1 and 10 μM did not influence Ca^{2+}-independent transporter-mediated synaptosomal release of [^{3}H] GABA

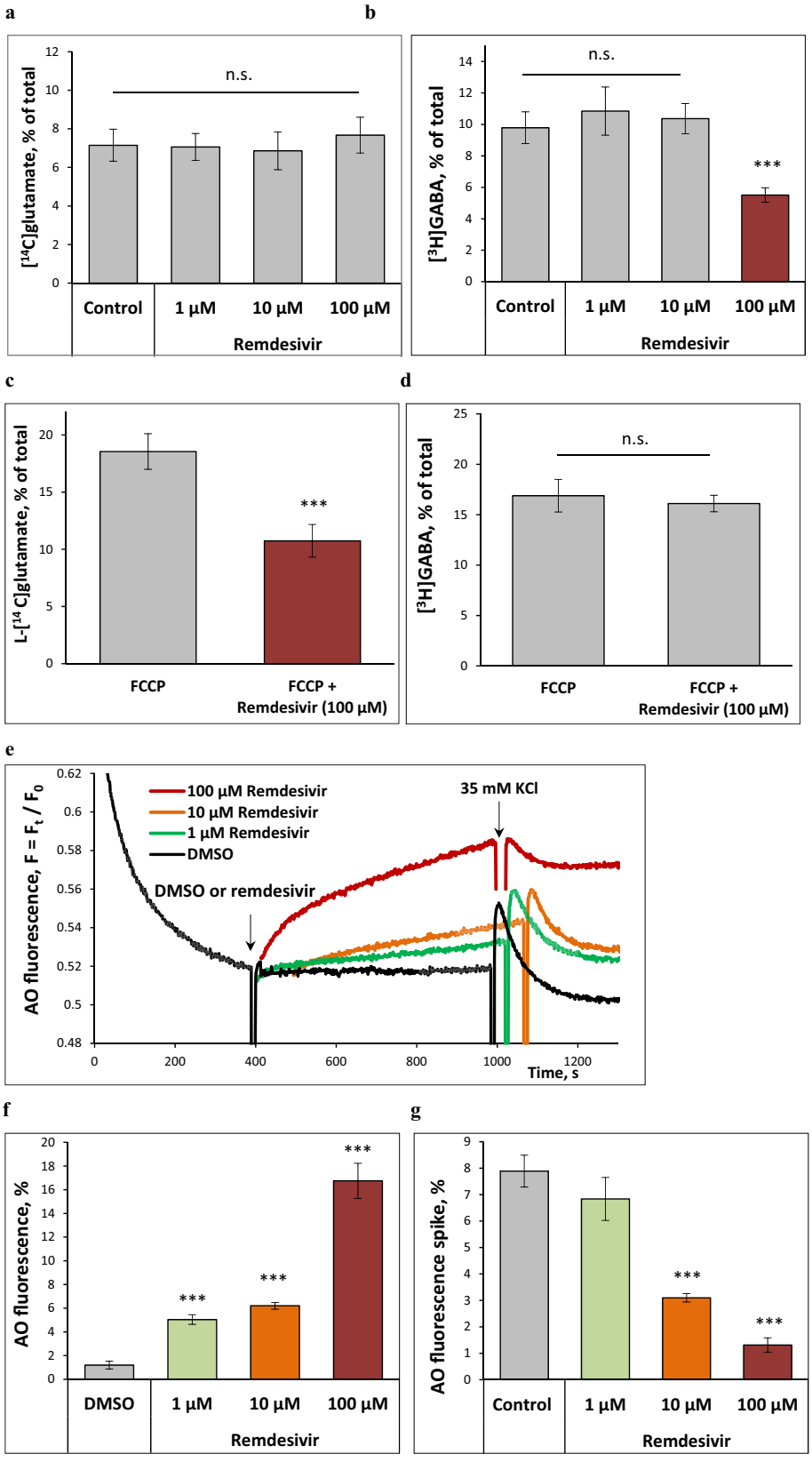

Fig. 5. a, b – Transporter-mediated release of L-[^{14}C] glutamate (a) and [^{3}H] GABA (b) from nerve terminals stimulated by the membrane depolarization with 35 mM KCl in Ca^{2+}-free media in the presence of remdesivir at concentrations of 1, 10, 100 μM. Data are the mean ± SEM. n.s., no significant differences; ***, $p < 0.001$, as compared to the control; $n = 12$.
c, d – FCCP-induced transporter-mediated release of L-[^{14}C] glutamate (c) and [^{3}H] GABA (d) from nerve terminals in the presence of remdesivir (100 μM). Data are the mean ± SEM. n.s., no significant differences; ***, $p < 0.001$, as compared to the control; $n = 12$.
e, f, g – Synaptic vesicle acidification in the presence of remdesivir at concentrations of 1, 10, 100 μM. e – The synaptosome suspension was equilibrated with 5 μM acridine orange, and when the steady level of the dye fluorescence was reached, DMSO or remdesivir (marked by arrow) were applied to synaptosomes. f – Calculation of changes in AO fluorescence in response to addition of DMSO or remdesivir. g – Calculation of changes in the spike of AO fluorescence in response to addition of 35 mM KCl during remdesivir administration. Data are mean ± SEM. ***, $p < 0.001$ as compared to the control; $n = 12$.

stimulated by 35 mM KCl that was 9.79 ± 1.01% of total synaptosome label in the control, 10.85 ± 1.53% of total synaptosome label in the presence of remdesivir at a concentration of 1 μM [$F_{(1,22)} = 0.36$; $p = 0.55$; $n = 12$], 10.37 ± 0.96% of total synaptosome label in the presence of remdesivir at a concentration of 10 μM [$F_{(1,22)} = 0.18$; $p = 0.67$; $n = 12$]. Whereas, remdesivir at a concentration of 100 μM decreased transporter-mediated release of [^{3}H] GABA that was equal to 5.51 ± 0.46% of total synaptosome label in the presence of remdesivir [$F_{(1,22)} = 14.95$; $p < 0.001$; $n = 12$] (Fig. 5b).

Therefore, remdesivir did not change the release of L-[^{14}C] glutamate via glutamate transporter reversal, but decreased that of [^{3}H] GABA starting from a concentration of 100 μM.

3.4.5. Synaptosomal transporter-mediated release of L-[^{14}C] glutamate and [^{3}H] GABA stimulated by the dissipation of the synaptic vesicle proton gradient during remdesivir administration

The classical protonophore carbonylcyanide *p*-trifluoromethoxyphenylhydrazone (FCCP) was used to dissipate the proton gradient of synaptic vesicles, thereby stimulating leakage of vesicular L-[^{14}C] glutamate and [^{3}H] GABA to the cytosol, and then to the extracellular space via transporter reversal.

Remdesivir at a concentration of 100 μM decreased the FCCP-stimulated release of L-[^{14}C] glutamate from nerve terminals that was 18.55 ± 1.56% of total synaptosome label in the control and 10.74 ± 1.43% of total synaptosome label in the presence of remdesivir [$F_{(1,22)} = 14.88$; $p < 0.001$; $n = 12$] (Fig. 5c). Remdesivir at a concentration of 100 μM did not change the FCCP-stimulated release of [^{3}H] GABA from nerve terminals. [^{3}H] GABA release was of 16.89 ± 1.62% of total synaptosome label in the control and 16.11 ± 0.82% of total synaptosome label in the presence of remdesivir [$F_{(1,22)} = 0.2$; $p = 0.66$; n = 12] (Fig. 5d).

3.4.6. Fluorescence assay: synaptic vesicle acidification during remdesivir administration

One of the causes of remdesivir-induced mitigation of exocytotic release can be changes in filling of synaptic vesicles with neurotransmitters that depends on the V-ATPase functioning and the proton gradient across the vesicle membrane. A pH-sensitive fluorescent dye acridine orange was applied to measure the synaptic vesicle acidification, as a component of the electrochemical proton gradient [52]. As shown in Fig. 5e, the addition of acridine orange to the nerve terminals caused a partial quenching of the fluorescence signal due to accumulation of acridine orange by synaptic vesicles. The steady state level of the dye fluorescence was achieved for 6 min, and this level was considered as 100% in further calculations. Application of remdesivir caused an immediate increase in the dye fluorescence, indicating a decrease in acidification of synaptic vesicles (Fig. 5e, f). Membrane depolarization using 35 mM KCl induced a spike of the dye fluorescence due to a temporal decrease in nerve terminal acidification associated with synaptic vesicle exocytosis followed by the acidification increase resulted from endocytosis. It was revealed a remdesivir-associated decrease in the fluorescence spike (Fig. 5e, g) that reflected a decrease in synaptic vesicle exocytosis, thereby confirming above experiments with radiolabeled neurotransmitters.

4. Discussion

To our knowledge current study is the first report of strong interaction of remdesivir with the cellular membrane and its deep incorporation in the lipid bilayer demonstrated by means of molecular dynamics simulations (Fig. 1a, b), BLMs technique (Fig. 2a, b) and FTIR spectroscopy (Fig. 3).

Viral envelopes consist of proteins and lipid components derived from the membranes of host cells [53]. Therefore, it can be hypothesized that remdesivir can incorporate into the viral envelopes in the same way as it incorporates into the membranes of the host cells. Virus is not capable to metabolize remdesivir, and so the latter can accumulate in the lipid bilayer of the viral envelope. One can speculate that the drug may even disturb proper functioning of envelope proteins, in particular S-glycoprotein of SARS-CoV-2 responsible for fusion of the viral envelope and host cell membrane [54] and influence the membrane fusion events, crucial for the virus life cycle. Although our results do not allow estimating such direct effects of remdesivir on viral membranes, it suggests that the virus envelope-targeted activity of remdesivir requires further detailed investigation.

Another major finding of this study is a remdesivir-induced decrease in exocytotic release of excitatory and inhibitory neurotransmitters from nerve terminals, which was dose-dependent and more strong in L-[^{14}C] glutamate experiments (Fig. 4 a) than in [^{3}H] GABA ones (Fig. 4b). Disturbance of the extracellular level of L-[^{14}C] glutamate was not a cause of exocytosis impairment, because remdesivir did not affect this parameter (Fig. 4c). Remdesivir acted differently in glutamate- and GABA-ergic nerve terminals attenuating the extracellular level of [^{3}H] GABA (Fig. 4d), thereby gaining a capability to mitigate synaptic inhibition. Importantly, unchanged tonic leakage of [^{3}H] GABA from nerve terminals measured during blockage of GABA transporter functioning (Fig. 4e) showed unchanged passive membrane permeability for the neurotransmitter in the presence of remdesivir. Data on the L-[^{14}C] glutamate uptake (Table 2) agreed with the extracellular level data (Fig. 4c) with no remdesivir effects on both parameters. Whereas, the drug decreased [^{3}H] GABA uptake in a dose-dependent manner starting from a concentration of 10 μM (Fig. 4f), thereby demonstrating diverse effects on uptake of excitatory and inhibitory neurotransmitters. Some discrepancy can be found between the extracellular level and uptake in [^{3}H] GABA experiments, namely remdesivir acted in a unidirectional manner on these parameters, whereas as usual these parameters demonstrated oppositely directed alterations in different studies, e.g. hypoxia model, exposure to neurotoxic and membrane active substances and nanoparticles [49,55–58] Transporter-mediated L-[^{14}C] glutamate release (Fig. 5a) was not changed by remdesivir, and so agreed with the above-mentioned extracellular level (Fig. 4c) and uptake data (Table 2). Whereas, remdesivir differently influenced this parameter in GABA-ergic nerve terminals and decreased transporter-mediated [^{3}H] GABA release staring from a concentration of 100 μM (Fig. 5b). [^{3}H] GABA data may be explained by decreased surface expression of GABA transporters due to impaired substrate-dependent regulation of GABA transporter functioning via protein kinase C-dependent mechanism in the presence of remdesivir. In this context, a decreased number or changed subtype distribution of functionally active GABA transporters may result in decreased uptake, reduced cytosolic pool of the neurotransmitter, and thus weakened transporter-mediated release, the extracellular level and turnover of neurotransmitter across the plasma membrane [59,60].

These effects of remdesivir may be due to its capability to form active nucleoside triphosphate [10] that can replace ATP molecule in ATP hydrolysis-dependent synaptic processes and ATP-associated receptor signalling, for instance, exocytosis, functioning of Na-K ATPase, V-ATPase, P2X7 receptors, etc. In particular, capability of remdesivir to interact with V-ATPase was predicted in computational modeling [61] that in turn may result in decreased synaptic vesicle acidification and decreased vesicular neurotransmitter content. Also, elevated extracellular levels of ATP evoked by SARS-CoV-2 infection may trigger hyperactivation of P2X7 receptors, which are ATP-gated ion channels widely expressed in the central nervous system [62]. In particular, P2X7 receptor activation evoked by viral infection led to alterations in reactive oxygen species formation, increased Ca^{2+} influx and glutamate release [63,64]. In turn, glutamate activates NMDA receptors expressed in nerve terminals, which determine Ca^{2+}-dependent exocytosis of ATP and more glutamate release, causing a massive release of the neurotransmitters augmenting excitotoxicity and cell death [1]. It can be suggested that remdesivir-derived nucleoside triphosphate may prevent hyperactivation of P2X7 receptors evoked by SARS-CoV-2, whereas this

suggestion needs to be further investigated.

Taking into account L-[^{14}C] glutamate results, it can be suggested that remdesivir did not provoke development of excitotoxicity because of an unchanged extracellular level, uptake and transporter reversal. However, a decreased extracellular level of [^{3}H] GABA may result in weakening synaptic inhibition and misbalance of excitatory and inhibitory signals.

Fluorimetric results using a pH-sensitive dye confirmed above experiments with radiolabeled neurotransmitters showing a decrease in exocytosis, one of the cause of which can be dissipated pH gradient across the synaptic vesicle membrane (Fig. 5e, f, g), which is the driving force for neurotransmitter accumulation, and so filling of synaptic vesicles with neurotransmitters. It should be noted that above fluorimetric studies demonstrated a cumulative response of all types of nerve terminals on remdesivir administration. In addition, it can be suggested that remdesivir can also dissipate the pH gradient of other intracellular acidic compartments, for instance, endosomal-lysosomal system involved in virus transportation. This can represent the additional mechanisms of virus-targeted action of remdesivir not only as RNA polymerase inhibitor, but also as modulator of intracellular virus transportation. Also, disturbance of exocytotic process per se can mitigate virus transmission.

Besides possible action of remdesivir in nerve terminals as a nucleoside analogue, the neurologic effects may be associated also with its amphiphilic properties and capability to interact with the membrane. The correlation of BLM and synaptic neurotransmission data was analyzed in our previous studies [56,65,66]. It was revealed that carbon nanodots (synthesized from β-alanine) and detonation nanodiamonds were capable of increasing the conductance of the BLM by inducing stable potential-dependent cation-selective pores. It was concluded that transmembrane BLM currents induced by both nanoparticles coincided with disturbance of neurotransmitter transport, in particular the extracellular concentrations of excitatory neurotransmitters L-[^{14}C]glutamate and D-[2,3^{3}H]aspartate, as well as inhibitory ones [^{3}H]GABA and [^{3}H]glycine in nerve terminal preparations. Simultaneously, both nanoparticles decreased acidification of synaptic vesicles [66]. In this context, it can be speculated that membrane active compounds/nanoparticles can change not only properties of the plasma membrane but also synaptic vesicle membrane presumably because of vesicle recycling. In other study, it was suggested that capacity of particles to affect integrity of nerve terminals and so key synaptic transmission characteristics may be evaluated using BLM by monitoring membrane conductivity in the presence of particles [56]. Also, pore-formation induced in the BLM by cationic biocide, polyhexamethylene guanidine hydrochloride, coincided with decreased exocytotic release and uptake of L-[^{14}C]glutamate and increased extracellular concentration of this neurotransmitter in nerve terminal preparations [65].

Taken together, our neurodata demonstrated for the first time that remdesivir starting from a concentration of 1 μM decreased depolarization-induced exocytotic release of L-[^{14}C] glutamate and [^{3}H] GABA in a dose-dependent manner. Remdesivir at concentrations of 1–100 μM did not change the extracellular level of L-[^{14}C] glutamate in nerve terminal preparations, but decreased this level of [^{3}H] GABA. Remdesivir did not affect L-[^{14}C] glutamate uptake, whereas it decreased [^{3}H] GABA uptake in a dose-dependent manner starting from a concentration of 10 μM, thereby demonstrating diverse effects on transportation of excitatory and inhibitory neurotransmitters. Tonic leakage of [^{3}H] GABA from nerve terminals measured in the presence of GABA transporter inhibitor NO-711 was not changed by the drug, thereby showing unchanged membrane permeability for this neurotransmitter. The drug did not change the release of L-[^{14}C] glutamate via glutamate transporter reversal, but decreased transporter-mediated [^{3}H] GABA release at a concentration of 100 μM. Protonophore FCCP-induced L-[^{14}C] glutamate release was decreased by remdesivir, but [^{3}H] GABA one remained unchanged. Fluorimetric studies using pH-sensitive dye acridine orange confirmed remdesivir-induced impairment of exocytosis and revealed a decrease in synaptic vesicle acidification.

A special attention should be paid to the fact that remdesivir and drug-derived material can be accumulated in the brain without changes in their concentrations during 7 days after administration [10]. It is clear that remdesivir concentrations must be precisely controlled during antiviral therapy, because the drug action can be accompanied by dysregulation of synaptic neurotransmission. Indeed, the literature data described usable remdesivir concentrations within the concentration ranges similar to this study. In patient treatment, remdesivir dosage was 200 mg intravenously on day 1 and 100 mg intravenously on day 2–10 [67,68]. In studies in vitro, active nucleoside triphosphate formation in human monocyte-derived macrophages was analyzed following 72-h incubation with 1 μM remdesivir [10]. Remdesivir inhibited acute Ebola virus replication in human cells including primary macrophages and human endothelial cells with half-maximum effective concentration (EC50) values of 0.06 to 0.14 μM.

Our data on changes in glutamate and GABA neurotransmission are in accordance with reported side effects of remdesivir, e.g. nervous system disorders (~3%) and psychiatric disorders (~1%) [69]. Identified neuropsychological toxicities of remdesivir were headache, anxiety, seizures, lethargy, delirious symptoms, and poor mental status [68,70–72]. Also, hypoxia (~2.5%) was shown as side effect of remdesivir [69] that in turn can significantly aggravate remdesivir-induced disturbance in neurotransmitter transport shown in our study. Other most common adverse events of remdesivir in the treatment of critically ill patients were increased hepatic enzymes, diarrhea, rash, renal impairment, hypotension, multiple-organ-dysfunction syndrome, and septic shock [68].

To date, many studies have been revealed the central nervous system toxicity in response to application of antiviral agents, which may cause severe neuropsychiatric complications, i.e. depression, psychosis, painful peripheral neuropathy, irritability, difficulty sleeping, etc. Neuropsychiatric effects of antiviral drugs are a common occurrence, which complicates treatment [73]. Pathogenetic mechanisms may involve different molecular targets, including $GABA_A$ receptors. Peripheral neuropathy for nucleoside and nucleotide analogues is more noticeable with higher dosage and prolonged duration of exposure [73]. Nucleotide analogues used to treat human immunodeficiency virus or hepatitis C virus can cause sensorineural peripheral neuropathy and other neurological toxicities [74,75]. It has been suggested that the reaction to most antiviral drugs is idiosyncratic, and the mechanisms of neuropsychiatric effects of these drugs are still unclear, and further research is warranted to elucidate this fact [73].

Drugs used in the palliative treatment of COVID-19 patients also have neurotoxic effects [76]. Antiretroviral drugs targeted coronavirus replication may produce undesirable effects on the central/peripheral nervous systems, variable in frequency and severity, depending on the involved molecular mechanisms [77]. Despite poor penetration through the blood-brain barrier, these drugs are essentially neurotoxic, showing perioral and peripheral paresthesias, and changes in taste within the first month of treatment [78]. In particular, the combination of lopinavir and ritonavir was associated with bilateral sensorineural hearing loss (in 4 weeks of treatment), and the appearance of depressive symptoms. In contrast, darunavir did not show increased neurotoxicity [77,78].

5. Conclusions

Direct membranotropic and neurotropic effects of remdesivir are shown for the first time. Remdesivir is able to accumulate in the cell membranes and affects lipid interactions. The drug decreases exocytotic release of L-[^{14}C] glutamate and [^{3}H] GABA from nerve terminals while not provoking development of excitotoxicity and not changing the passive membrane permeability for neurotransmitters. Decreased extracellular level of [^{3}H] GABA after drug administration may weaken synaptic inhibition and change the balance of excitatory and inhibitory

signals. The drug decreases synaptic vesicle acidification that can be one of the causes of decreased exocytosis.

As remdesivir and its active metabolite can accumulate in the brain, the remdesivir dosing during antiviral therapy should be controlled carefully due to possible unwanted modulation of excitatory and inhibitory synaptic neurotransmission.

Ethics approval

All procedures were conducted according to ARRIVE guidelines for reporting experiments involving animals [39]. Experimental protocols were approved by the Animal Care and Use Committee of the Palladin Institute of Biochemistry (Protocol from September 21, 2020).

Authors' contributions

GD, SY, KP, TB – conceptualisation and project writing; AP – isolation of synaptosomes; AP and NK – L-[^{14}C] glutamate uptake and release measurements and fluorimetry; NP and MD – [^{3}H] GABA uptake and release measurements; SY – molecular dynamics simulations; GD, OG, UA – FTIR spectroscopy; OS-planar lipid bilayer experiments; NP, NK, TB – data analysis; NP, SY, GD, OG – figure preparation; TB – the design of the neurochemical study and draft manuscript writing. The manuscript was edited by TB, GD and SY. All authors read and approved the final manuscript.

Declaration of competing interest

The authors declare no financial and non-financial competing interests exist.

Data availability

No data was used for the research described in the article.

Acknowledgements

This work was supported by the National Research Foundation of Ukraine, Project #2020.01/0043 (authors - grant participants: NK, NP, AP, GD, OG, KP, SY, TB). The computational resources were provided by the Centre de calcul Champagne-Ardenne Romeo and the Mésocentre de calcul de Franche-Comté.

References

[1] D.E. Ribeiro, Á. Oliveira-Giacomelli, T. Glaser, V.F. Arnaud-Sampaio, R. Andrejew, L. Dieckmann, J. Baranova, C. Lameu, M.Z. Ratajczak, H. Ulrich, Hyperactivation of P2X7 receptors as a culprit of COVID-19 neuropathology, Mol. Psychiatry 26 (2020) 1044–1059, https://doi.org/10.1038/s41380-020-00965-3.

[2] A. Pezzini, A. Padovani, Lifting the mask on neurological manifestations of COVID-19, Nat. Rev. Neurol. 16 (2020) 636–644, https://doi.org/10.1038/s41582-020-0398-3.

[3] J. Netland, D.K. Meyerholz, S. Moore, M. Cassell, S. Perlman, Severe acute respiratory syndrome coronavirus infection causes neuronal death in the absence of encephalitis in mice transgenic for human ACE2, J. Virol. 82 (2008) 7264–7275, https://doi.org/10.1128/jvi.00737-08.

[4] K. Li, C. Wohlford-Lenane, S. Perlman, J. Zhao, A.K. Jewell, L.R. Reznikov, K. N. Gibson-Corley, D.K. Meyerholz, P.B. McCray, Middle east respiratory syndrome coronavirus causes multiple organ damage and lethal disease in mice transgenic for human dipeptidyl peptidase 4, J. Infect. Dis. 212 (2015) 712–722, https://doi.org/10.1093/infdis/jiv499.

[5] Y.C. Li, W.Z. Bai, T. Hashikawa, The neuroinvasive potential of SARS-CoV2 may play a role in the respiratory failure of COVID-19 patients, J. Med. Virol. 92 (2020) 552–555, https://doi.org/10.1002/jmv.25728.

[6] Y.C. Li, W.Z. Bai, N. Hirano, T. Hayashida, T. Taniguchi, Y. Sugita, K. Tohyama, T. Hashikawa, Neurotropic virus tracing suggests a membranous-coating-mediated mechanism for transsynaptic communication, J. Comp. Neurol. 521 (2013) 203–212, https://doi.org/10.1002/cne.23171.

[7] J.M. Kim, Y.S. Chung, H.J. Jo, N.J. Lee, M.S. Kim, S.H. Woo, S. Park, J.W. Kim, H. M. Kim, M.G. Han, Identification of coronavirus isolated from a patient in Korea with covid-19, Osong Public Heal. Res. Perspect. 11 (2020) 3–7, https://doi.org/10.24171/j.phrp.2020.11.1.02.

[8] R.T. Eastman, J.S. Roth, K.R. Brimacombe, A. Simeonov, M. Shen, S. Patnaik, M. D. Hall, Remdesivir: a review of its discovery and development leading to emergency use authorization for treatment of COVID-19, ACS Cent. Sci. 6 (2020) 672–683, https://doi.org/10.1021/acscentsci.0c00489.

[9] FDA, News release. May 1, 2020. Remdesivir EUA letter of authorization. https://www.fda.gov/media/137564/download, 2020 (accessed June 10, 2021).

[10] T.K. Warren, R. Jordan, M.K. Lo, A.S. Ray, R.L. Mackman, V. Soloveva, D. Siegel, M. Perron, R. Bannister, H.C. Hui, N. Larson, R. Strickley, J. Wells, K.S. Stuthman, S.A. Van Tongeren, N.L. Garza, G. Donnelly, A.C. Shurtleff, C.J. Retterer, D. Gharaibeh, R. Zamani, T. Kenny, B.P. Eaton, E. Grimes, L.S. Welch, L. Gomba, C. L. Wilhelmsen, D.K. Nichols, J.E. Nuss, E.R. Nagle, J.R. Kugelman, G. Palacios, E. Doerffler, S. Neville, E. Carra, M.O. Clarke, L. Zhang, W. Lew, B. Ross, Q. Wang, K. Chun, L. Wolfe, D. Babusis, Y. Park, K.M. Stray, I. Trancheva, J.Y. Feng, O. Barauskas, Y. Xu, P. Wong, M.R. Braun, M. Flint, L.K. McMullan, S.S. Chen, R. Fearns, S. Swaminathan, D.L. Mayers, C.F. Spiropoulou, W.A. Lee, S.T. Nichol, T. Cihlar, S. Bavari, Therapeutic efficacy of the small molecule GS-5734 against ebola virus in rhesus monkeys, Nature 531 (2016) 381–385, https://doi.org/10.1038/nature17180.

[11] T.C. Sudhof, The synaptic vesicle cycle, Annu. Rev. Neurosci. 27 (2004) 509–547, https://doi.org/10.1146/annurev.neuro.26.041002.131412.

[12] S. Jo, T. Kim, V.G. Iyer, W. Im, CHARMM-GUI: a web-based graphical user interface for CHARMM, J. Comput. Chem. 29 (2008) 1859–1865, https://doi.org/10.1002/jcc.20945.

[13] J. Lee, X. Cheng, J.M. Swails, M.S. Yeom, P.K. Eastman, J.A. Lemkul, S. Wei, J. Buckner, J.C. Jeong, Y. Qi, S. Jo, V.S. Pande, D.A. Case, C.L. Brooks, A. D. MacKerell, J.B. Klauda, W. Im, CHARMM-GUI input generator for NAMD, GROMACS, AMBER, OpenMM, and CHARMM/OpenMM simulations using the CHARMM36 additive force field, J. Chem. Theory Comput. 12 (2016) 405–413, https://doi.org/10.1021/acs.jctc.5b00935.

[14] M. Valiev, E.J. Bylaska, N. Govind, K. Kowalski, T.P. Straatsma, H.J.J. Van Dam, D. Wang, J. Nieplocha, E. Apra, T.L. Windus, W.A. De Jong, NWChem: a comprehensive and scalable open-source solution for large scale molecular simulations, Comput. Phys. Commun. 181 (2010) 1477–1489, https://doi.org/10.1016/j.cpc.2010.04.018.

[15] L. Botto, E. Beretta, R. Daffara, G. Miserocchi, P. Palestini, Biochemical and morphological changes in endothelial cells in response to hypoxic interstitial edema, Respir. Res. 7 (2006) 7, https://doi.org/10.1186/1465-9921-7-7.

[16] N. Zehethofer, S. Bermbach, S. Hagner, H. Garn, J. Müller, T. Goldmann, B. Lindner, D. Schwudke, P. König, Lipid analysis of airway epithelial cells for studying respiratory diseases, Chromatographia 78 (2015) 403–413, https://doi.org/10.1007/s10337-014-2787-5.

[17] K.A. Zemski Berry, R.C. Murphy, B. Kosmider, R.J. Mason, Lipidomic characterization and localization of phospholipids in the human lung, J. Lipid Res. 58 (2017) 926–933, https://doi.org/10.1194/jlr.M074955.

[18] S.O. Yesylevskyy, S. Kraszewski, C. Ramseyer, Determination of the shape and curvature of nonplanar lipid bilayers that are bent in a single plane in molecular dynamics simulations, J. Mol. Model. 20 (2014) 2176, https://doi.org/10.1007/s00894-014-2176-x.

[19] S.O. Yesylevskyy, C. Ramseyer, Determination of mean and gaussian curvatures of highly curved asymmetric lipid bilayers: the case study of the influence of cholesterol on the membrane shape, Phys. Chem. Chem. Phys. 16 (2014) 17052–17061, https://doi.org/10.1039/c4cp01544d.

[20] T. Rivel, C. Ramseyer, S.O. Yesylevskyy, Permeation of Cisplatin Through the Membranes of Normal and Cancer Cells: A Molecular Dynamics Study, BioRxiv, 2018, https://doi.org/10.1101/375980.

[21] T. Rivel, C. Ramseyer, S. Yesylevskyy, The asymmetry of plasma membranes and their cholesterol content influence the uptake of cisplatin, Sci. Rep. 9 (2019) 5627, https://doi.org/10.1038/s41598-019-41903-w.

[22] S. Yesylevskyy, T. Rivel, C. Ramseyer, Curvature increases permeability of the plasma membrane for ions, water and the anti-cancer drugs cisplatin and gemcitabine, Sci. Rep. 9 (2019) 17214, https://doi.org/10.1038/s41598-019-53952-2.

[23] S.O. Yesylevskyy, T. Rivel, C. Ramseyer, The influence of curvature on the properties of the plasma membrane. Insights from atomistic molecular dynamics simulations, Sci. Rep. 7 (2017) 16078, https://doi.org/10.1038/s41598-017-16450-x.

[24] S. Yesylevskyy, H. Khandelia, EnCurv: simple technique of maintaining global membrane curvature in molecular dynamics simulations, J. Chem. Theory Comput. 17 (2021) 1181–1193, https://doi.org/10.1021/acs.jctc.0c00800.

[25] B. Hess, C. Kutzner, D. Van Der Spoel, E. Lindahl, GRGMACS 4: algorithms for highly efficient, load-balanced, and scalable molecular simulation, J. Chem. Theory Comput. 4 (2008) 435–447, https://doi.org/10.1021/ct700301q.

[26] G.A. Tribello, M. Bonomi, D. Branduardi, C. Camilloni, G. Bussi, PLUMED 2: new feathers for an old bird, Comput. Phys. Commun. 185 (2014) 604–613, https://doi.org/10.1016/j.cpc.2013.09.018.

[27] M. Bonomi, G. Bussi, C. Camilloni, G.A. Tribello, P. Banáš, A. Barducci, M. Bernetti, P.G. Bolhuis, S. Bottaro, D. Branduardi, R. Capelli, P. Carloni, M. Ceriotti, A. Cesari, H. Chen, W. Chen, F. Colizzi, S. De, M. De La Pierre, D. Donadio, V. Drobot, B. Ensing, A.L. Ferguson, M. Filizola, J.S. Fraser, H. Fu, P. Gasparotto, F. L. Gervasio, F. Giberti, A. Gil-Ley, T. Giorgino, G.T. Heller, G.M. Hocky, M. Iannuzzi, M. Invernizzi, K.E. Jelfs, A. Jussupow, E. Kirilin, A. Laio, V. Limongelli, K. Lindorff-Larsen, T. Löhr, F. Marinelli, L. Martin-Samos, M. Masetti, R. Meyer, A. Michaelides, C. Molteni, T. Morishita, M. Nava, C. Paissoni, E. Papaleo, M. Parrinello, J. Pfaendtner, P. Piaggi, G.M. Piccini, A. Pietropaolo, F. Pietrucci, S. Pipolo, D. Provasi, D. Quigley, P. Raiteri, S. Raniolo, J. Rydzewski, M. Salvalaglio, G.C. Sosso, V. Spiwok, J. Šponer, D.W.H. Swenson,

P. Tiwary, O. Valsson, M. Vendruscolo, G.A. Voth, A. White, Promoting transparency and reproducibility in enhanced molecular simulations, Nat. Methods 16 (2019) 670–673, https://doi.org/10.1038/s41592-019-0506-8.
[28] J. Huang, A.D. Mackerell, CHARMM36 all-atom additive protein force field: validation based on comparison to NMR data, J. Comput. Chem. 34 (2013) 2135–2145, https://doi.org/10.1002/jcc.23354.
[29] H.J.C. Berendsen, J.P.M. Postma, W.F. Van Gunsteren, A. Dinola, J.R. Haak, Molecular dynamics with coupling to an external bath, J. Chem. Phys. 81 (1984) 3684–3690, https://doi.org/10.1063/1.448118.
[30] Y.K. Cherniavskyi, C. Ramseyer, S.O. Yesylevskyy, Interaction of C60 fullerenes with asymmetric and curved lipid membranes: a molecular dynamics study, Phys. Chem. Chem. Phys. 18 (2016) 278–284, https://doi.org/10.1039/c5cp05838d.
[31] S. Páll, B. Hess, A flexible algorithm for calculating pair interactions on SIMD architectures, Comput. Phys. Commun. 184 (2013) 2641–2650, https://doi.org/10.1016/j.cpc.2013.06.003.
[32] D. Van Der Spoel, E. Lindahl, B. Hess, G. Groenhof, A.E. Mark, H.J.C. Berendsen, GROMACS: fast, flexible, and free, J. Comput. Chem. 26 (2005) 1701–1718, https://doi.org/10.1002/jcc.20291.
[33] G. Bussi, D. Donadio, M. Parrinello, Canonical sampling through velocity rescaling, J. Chem. Phys. 126 (2007), 014101, https://doi.org/10.1063/1.2408420.
[34] S.O. Yesylevskyy, Pteros 2.0: evolution of the fast parallel molecular analysis library for C++ and python, J. Comput. Chem. 36 (2015) 1480–1488, https://doi.org/10.1002/jcc.23943.
[35] S.O. Yesylevskyy, Pteros: fast and easy to use open-source C++ library for molecular analysis, J. Comput. Chem. 33 (2012) 1632–1636, https://doi.org/10.1002/jcc.22989.
[36] W. Humphrey, A. Dalke, K. Schulten, VMD: visual molecular dynamics, J. Mol. Graph. 14 (1996) 33–38, https://doi.org/10.1016/0263-7855(96)00018-5.
[37] P. Mueller, D.O. Rudin, H. Ti Tien, W.C. Wescott, Reconstitution of cell membrane structure in vitro and its transformation into an excitable system, Nature 194 (1962) 979–980, https://doi.org/10.1038/194979a0.
[38] C. Kilkenny, W. Browne, I.C. Cuthill, M. Emerson, D.G. Altman, NC3Rs reporting guidelines working group, animal research: reporting in vivo experiments: the ARRIVE guidelines, Br. J. Pharmacol. 160 (2010) 1577–1579, https://doi.org/10.1111/j.1476-5381.2010.00872.x.
[39] J.C. McGrath, G.B. Drummond, E.M. McLachlan, C. Kilkenny, C.L. Wainwright, Guidelines for reporting experiments involving animals: the ARRIVE guidelines, Br. J. Pharmacol. 160 (2010) 1573–1576, https://doi.org/10.1111/j.1476-5381.2010.00873.x.
[40] C.W. Cotman, Isolation of synaptosomal and synaptic plasma membrane fractions, Methods Enzymol. 31 (1974) 445–452 (accessed April 21, 2017), http://www.ncbi.nlm.nih.gov/pubmed/4278474.
[41] T. Borisova, The neurotoxic effects of heavy metals: alterations in acidification of synaptic vesicles and glutamate transport in brain nerve terminals, Horizons Neurosci. Res. 14 (2014) 89–112.
[42] A. Borysov, N. Krisanova, O. Chunihin, L. Ostapchenko, N. Pozdnyakova, T. Borisova, A comparative study of neurotoxic potential of synthesized polysaccharide-coated and native ferritin-based magnetic nanoparticles, Croat. Med. J. 55 (2014) 195–205, https://doi.org/10.3325/cmj.2014.55.195.
[43] E. Larson, B. Howlett, A. Jagendorf, Artificial reductant enhancement of the Lowry method for protein determination, Anal. Biochem. 155 (1986) 243–248 (accessed April 21, 2017), http://www.ncbi.nlm.nih.gov/pubmed/3728976.
[44] T. Borisova, A. Nazarova, M. Dekaliuk, N. Krisanova, N. Pozdnyakova, A. Borysov, R. Sivko, A.P. Demchenko, Neuromodulatory properties of fluorescent carbon dots: effect on exocytotic release, uptake and ambient level of glutamate and GABA in brain nerve terminals, Int. J. Biochem. Cell Biol. 59 (2015) 203–215, https://doi.org/10.1016/j.biocel.2014.11.016.
[45] T. Borisova, N. Pozdnyakova, N. Krisanova, A. Pastukhov, M. Dudarenko, K. Paliienko, V. Grytsaenko, F. Lux, V. Lysenko, P. Rocchi, S. Komisarenko, O. Tillement, Unique features of brain metastases-targeted AGuIX nanoparticles vs their constituents: a focus on glutamate-/GABA-ergic neurotransmission in cortex nerve terminals, Food Chem. Toxicol. 149 (2021), 112004, https://doi.org/10.1016/j.fct.2021.112004.
[46] N. Krisanova, N. Pozdnyakova, A. Pastukhov, M. Dudarenko, O. Maksymchuk, P. Parkhomets, R. Sivko, T. Borisova, Vitamin D3 deficiency in puberty rats causes presynaptic malfunctioning through alterations in exocytotic release and uptake of glutamate/GABA and expression of EAAC-1/GAT-3 transporters, Food Chem. Toxicol. 123 (2019) 142–150, https://doi.org/10.1016/j.fct.2018.10.054.
[47] N. Pozdnyakova, A. Pastukhov, M. Dudarenko, M. Galkin, A. Borysov, T. Borisova, Neuroactivity of detonation nanodiamonds: dose-dependent changes in transporter-mediated uptake and ambient level of excitatory/inhibitory neurotransmitters in brain nerve terminals, J. Nanobiotechnol. 14 (2016) 25, https://doi.org/10.1186/s12951-016-0176-y.
[48] O. Soldatkin, A. Nazarova, N. Krisanova, A. Borysov, D. Kucherenko, I. Kucherenko, N. Pozdnyakova, A. Soldatkin, T. Borisova, Monitoring of the velocity of high-affinity glutamate uptake by isolated brain nerve terminals using amperometric glutamate biosensor, Talanta 135 (2015) 67–74, https://doi.org/10.1016/j.talanta.2014.12.031.
[49] N. Pozdnyakova, Consequences of perinatal hypoxia in developing brain: changes in GABA transporter functioning in cortical, hippocampal and thalamic rat nerve terminals, Int. J. Dev. Neurosci. 63 (2017) 1–7, https://doi.org/10.1016/j.ijdevneu.2017.09.002.
[50] A.S. Tarasenko, R.V. Sivko, N.V. Krisanova, N.H. Himmelreich, T.A. Borisova, Cholesterol depletion from the plasma membrane impairs proton and glutamate storage in synaptic vesicles of nerve terminals, J. Mol. Neurosci. 41 (2010) 358–367, https://doi.org/10.1007/s12031-010-9351-z.
[51] A.E. Shamoo, D.A. Goldstein, Isolation of ionophores from ion transport systems and their role in energy transduction, Biochim. Biophys. Acta Rev. Biomembr. 472 (1977) 13–53, https://doi.org/10.1016/0304-4157(77)90013-2.
[52] F. Zoccarato, L. Cavallini, A. Alexandre, The pH-sensitive dye acridine orange as a tool to monitor exocytosis/endocytosis in synaptosomes, J. Neurochem. 72 (1999) 625–633 (accessed August 30, 2017), http://www.ncbi.nlm.nih.gov/pubmed/9930734.
[53] J.K. Millet, G.R. Whittaker, Physiological and molecular triggers for SARS-CoV membrane fusion and entry into host cells, Virology 517 (2018) 3–8, https://doi.org/10.1016/j.virol.2017.12.015.
[54] J. Glende, C. Schwegmann-Wessels, M. Al-Falah, S. Pfefferle, X. Qu, H. Deng, C. Drosten, H.Y. Naim, G. Herrler, Importance of cholesterol-rich membrane microdomains in the interaction of the S protein of SARS-coronavirus with the cellular receptor angiotensin-converting enzyme 2, Virology 381 (2008) 215–221, https://doi.org/10.1016/j.virol.2008.08.026.
[55] N. Pozdnyakova, M. Dudarenko, T. Borisova, Age-dependency of levetiracetam effects on exocytotic GABA release from nerve terminals in the hippocampus and cortex in norm and after perinatal hypoxia, Cell. Mol. Neurobiol. 39 (2019) 701–714, https://doi.org/10.1007/s10571-019-00676-6.
[56] T. Borisova, Express assessment of neurotoxicity of particles of planetary and interstellar dust, Npj Microgravity 5 (2019) 2, https://doi.org/10.1038/s41526-019-0062-7.
[57] T. Borisova, Nervous system injury in response to contact with environmental, engineered and planetary micro- and nano-sized particles, Front. Physiol. 9 (2018) 728, https://doi.org/10.3389/fphys.2018.00728.
[58] N. Pozdnyakova, N. Krisanova, M. Dudarenko, E. Vavers, L. Zvejniece, M. Dambrova, T. Borisova, Inhibition of sigma-1 receptors substantially modulates GABA and glutamate transport in presynaptic nerve terminals, Exp. Neurol. 333 (2020), 113434, https://doi.org/10.1016/j.expneurol.2020.113434.
[59] T. Borisova, Permanent dynamic transporter-mediated turnover of glutamate across the plasma membrane of presynaptic nerve terminals: arguments in favor and against, Rev. Neurosci. 27 (2016) 71–81, https://doi.org/10.1515/revneuro-2015-0023.
[60] T. Borisova, A. Borysov, Putative duality of presynaptic events, Rev. Neurosci. 27 (2016) 377–383 (accessed April 22, 2017), https://www.degruyter.com/view/j/revneuro.ahead-of-print/revneuro-2015-0044/revneuro-2015-0044.xml.
[61] A.O. Adeoye, B.J. Oso, I.F. Olaoye, H. Tijjani, A.I. Adebayo, Repurposing of chloroquine and some clinically approved antiviral drugs as effective therapeutics to prevent cellular entry and replication of coronavirus, J. Biomol. Struct. Dyn. (2020) 1–11, https://doi.org/10.1080/07391102.2020.1765876.
[62] R. Sluyter, The P2X7 receptor, in: Adv. Exp. Med. Biol, Springer New York LLC, 2017, pp. 17–53, https://doi.org/10.1007/5584_2017_59.
[63] M.Z. Ratajczak, A. Mack, K. Bujko, A. Domingues, D. Pedziwiatr, M. Kucia, J. Ratajczak, H. Ulrich, J. Kucharska-Mazur, J. Samochowiec, ATP-Nlrp3 inflammasome-complement Cascade Axis in sterile brain inflammation in psychiatric patients and its impact on stem cell trafficking, Stem Cell Rev. Rep. 15 (2019) 497–505, https://doi.org/10.1007/s12015-019-09888-1.
[64] E. Adinolfi, A.L. Giuliani, E. De Marchi, A. Pegoraro, E. Orioli, F. Di Virgilio, The P2X7 receptor: a main player in inflammation, Biochem. Pharmacol. 151 (2018) 234–244, https://doi.org/10.1016/j.bcp.2017.12.021.
[65] K.O. Paliienko, T.O. Veklich, O.Y. Shatursky, O.A. Shkrabak, A.O. Pastukhov, M. O. Galkin, N.V. Krisanova, A.J. Chunikhin, A.V. Rebriev, A.V. Lysytsya, T. A. Borisova, S.O. Kosterin, Membrane action of polyhexamethylene guanidine hydrochloride revealed on smooth muscle cells, nerve tissue and rat blood platelets: a biocide driven pore-formation in phospholipid bilayers, Toxicol. in Vitro 60 (2019) 389–399, https://doi.org/10.1016/j.tiv.2019.06.008.
[66] O.Y. Shatursky, A.P. Demchenko, I. Panas, N. Krisanova, N. Pozdnyakova, T. Borisova, The ability of carbon nanoparticles to increase transmembrane current of cations coincides with impaired synaptic neurotransmission, Biochim. Biophys. Acta - Biomembr. 1864 (2022), 183817, https://doi.org/10.1016/j.bbamem.2021.183817.
[67] C.J. Yang, Y.J. Wei, H.L. Chang, P.Y. Chang, C.C. Tsai, Y.H. Chen, P.R. Hsueh, Remdesivir use in the coronavirus disease 2019 pandemic: a mini-review, J. Microbiol. Immunol. Infect. 54 (2021) 27–36, https://doi.org/10.1016/j.jmii.2020.09.002.
[68] J. Grein, N. Ohmagari, D. Shin, G. Diaz, E. Asperges, A. Castagna, T. Feldt, G. Green, M.L. Green, F.-X. Lescure, E. Nicastri, R. Oda, K. Yo, E. Quiros-Roldan, A. Studemeister, J. Redinski, S. Ahmed, J. Bernett, D. Chelliah, D. Chen, S. Chihara, S.H. Cohen, J. Cunningham, A. D'Arminio Monforte, S. Ismail, H. Kato, G. Lapadula, E. L'Her, T. Maeno, S. Majumder, M. Massari, M. Mora-Rillo, Y. Mutoh, D. Nguyen, E. Verweij, A. Zoufaly, A.O. Osinusi, A. DeZure, Y. Zhao, L. Zhong, A. Chokkalingam, E. Elboudwarej, L. Telep, L. Timbs, I. Henne, S. Sellers, H. Cao, S.K. Tan, L. Winterbourne, P. Desai, R. Mera, A. Gaggar, R.P. Myers, D. M. Brainard, R. Childs, T. Flanigan, Compassionate use of remdesivir for patients with severe Covid-19, N. Engl. J. Med. 382 (2020) 2327–2336, https://doi.org/10.1056/nejmoa2007016.
[69] J. Charan, R.J. Kaur, P. Bhardwaj, M. Haque, P. Sharma, S. Misra, B. Godman, Rapid review of suspected adverse drug events due to remdesivir in the WHO database; findings and implications, Expert. Rev. Clin. Pharmacol. 14 (2021) 95–103, https://doi.org/10.1080/17512433.2021.1856655.
[70] S. Lee, J.W. Yang, S.Y. Jung, M.S. Kim, D.K. Yon, S.W. Lee, H.C. Kang, E. Dragioti, K. Tizaoui, L. Jacob, A. Koyanagi, J.E. Salem, K. Kostev, A. Lascu, J.I. Shin, J. H. Kim, L. Smith, Neuropsychological adverse drug reactions of remdesivir: analysis using VigiBase, the WHO global database of individual case safety reports, Eur. Rev. Med. Pharmacol. Sci. 25 (2021) 7390–7397, https://doi.org/10.26355/eurrev_202112_27435.

[71] A. Barlow, K.M. Landolf, B. Barlow, S.Y.A. Yeung, J.J. Heavner, C.W. Claassen, M. S. Heavner, Review of emerging pharmacotherapy for the treatment of Coronavirus Disease 2019, Pharmacother. J. Hum. Pharmacol. Drug Ther. 40 (2020) 416–437, https://doi.org/10.1002/phar.2398.

[72] P. Anand, K.H.V. Lau, D.Y. Chung, D. Virmani, A.M. Cervantes-Arslanian, A. Z. Mian, C.E. Takahashi, Posterior reversible encephalopathy syndrome in patients with coronavirus disease 2019: two cases and a review of the literature, J. Stroke Cerebrovasc. Dis. 29 (2020), 105212, https://doi.org/10.1016/j.jstrokecerebrovasdis.2020.105212.

[73] N. Zareifopoulos, M. Lagadinou, A. Karela, O. Kyriakopoulou, D. Velissaris, Neuropsychiatric effects of antiviral drugs, Cureus 12 (2020), e9536, https://doi.org/10.7759/cureus.9536.

[74] C.L. Cherry, J.C. McArthur, J.F. Hoy, S.L. Wesselingh, Nucleoside analogues and neuropathy in the era of HAART, J. Clin. Virol. 26 (2003) 195–207, https://doi.org/10.1016/S1386-6532(02)00118-X.

[75] S. Kiwuwa-Muyingo, B. Kikaire, I. Mambule, H. Musana, G. Musoro, C.F. Gilks, J. B. Levin, A.S. Walker, Prevalence, incidence and predictors of peripheral neuropathy in african adults with HIV infection within the DART trial, AIDS 28 (2014) 2579–2588, https://doi.org/10.1097/QAD.0000000000000447.

[76] B. Ünlü, R. Simsek, S.B.E. Köse, A. Yirün, P. Erkekoglu, Neurological effects of SARS-CoV-2 and neurotoxicity of antiviral drugs against COVID-19, Mini-Rev. Med. Chem. 22 (2021) 213–231, https://doi.org/10.2174/1389557521666210629100630.

[77] C.A.C. García, E.B.A. Sánchez, D.H. Huerta, J. Gómez-Arnau, Covid-19 treatment-induced neuropsychiatric adverse effects, Gen. Hosp. Psychiatry 67 (2020) 163–164, https://doi.org/10.1016/j.genhosppsych.2020.06.001.

[78] M.S. Abers, W.X. Shandera, J.S. Kass, Neurological and psychiatric adverse effects of antiretroviral drugs, CNS Drugs 28 (2014) 131–145, https://doi.org/10.1007/s40263-013-0132-4.